Density Functional Theory Study of In_2O_3-based Transparent Conductive Oxides

A First Principles Approach

Max van Duffelen

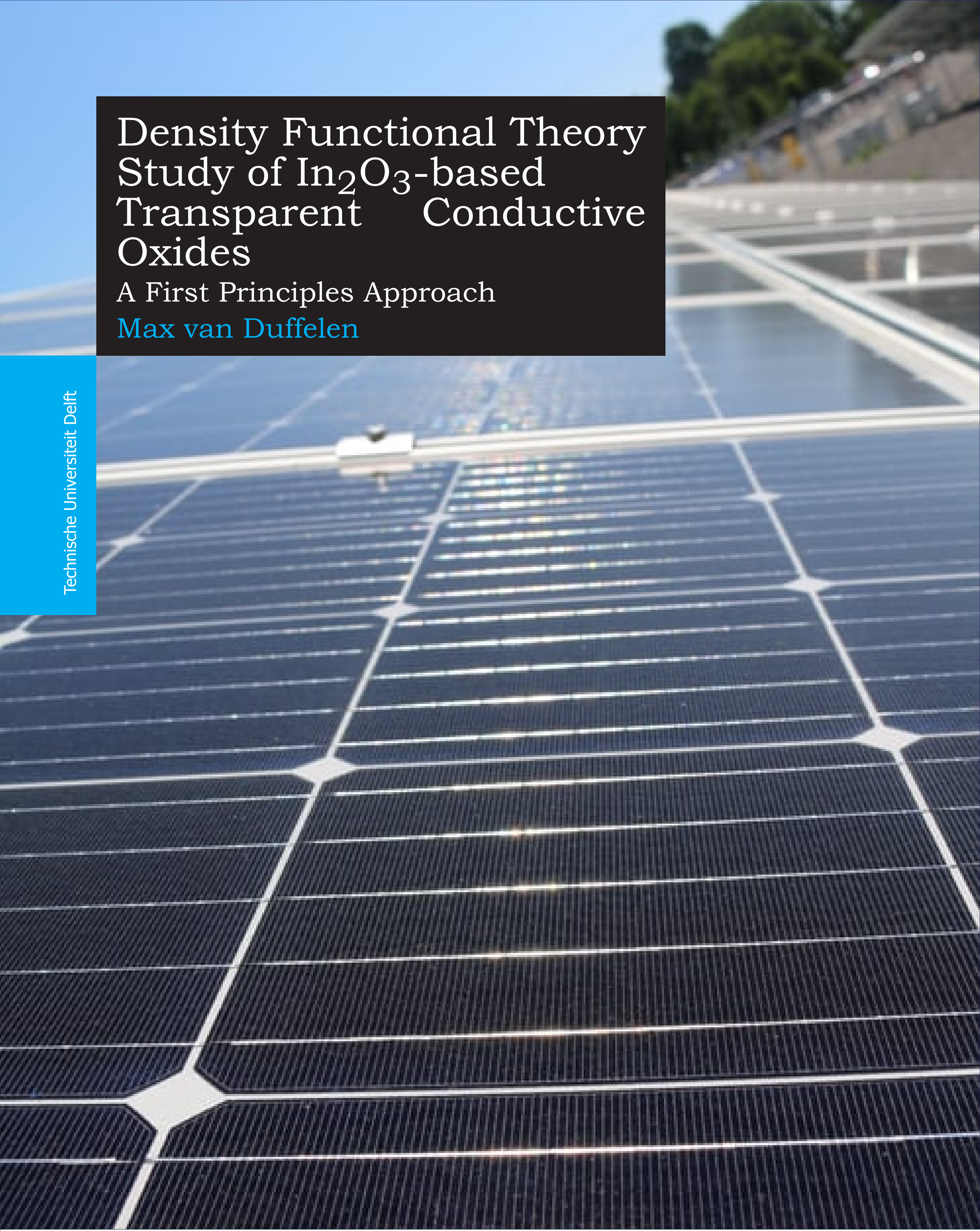

Technische Universiteit Delft

TU Delft
Delft
University of
Technology

Challenge the future

Density Functional Theory Study of In_2O_3-based Transparent Conductive Oxides

A First Principles Approach

by

Max van Duffelen

in partial fulfillment of the requirements for the degree of

Master of Science
in Sustainable Energy Technology

at the Delft University of Technology,
to be defended publicly on Thursday July 15, 2021 at 15:00 PM

Student number:	4369076		
Project duration:	November 2020 – July 2021		
Thesis Committee:	Dr. Rudi Santbergen	TU Delft, PVMD - EWI	Supervisor
	Ir. C. Han	TU Delft, PVMD - EWI	Daily Supervisor
	Dr. O. Isabella	TU Delft, PVMD - EWI	Internal Committee Member
	Prof. F.C. Grozema	TU Delft, CE - TNW	External Committee Member

Delft
University of
Technology

Abstract

Transparent conductive oxides (TCOs) play important roles in information and energy technologies. In the photovoltaic (PV) community, they are normally required to provide sufficient lateral carrier transport towards metal electrodes at the illumination side. Thus, a trade-off between optical and electrical properties is of critical importance in relevant device fabrications. So far, within the PVMD group, the investigation on TCOs has been mainly focused from an experimental perspective. In this thesis, a first-principles approach based on DFT software is investigated to obtain the self-consistent opto-electrical properties of TCOs.

A comprehensive study is carried out to understand the fundamentals of DFT software, as this is crucial to get reliable results from it. Within the PVMD group, the DFT method is applied on the indium-oxide (IO) host material. It was found that referable results for the (partial) density of states and band structure could be obtained for this structure using the *PBE* exchange-correlation (XC) functional. The dielectric function could be obtained by combining the *PBE* and *HSE06* XC functional through the PHS-method.

Based on a preliminary validation of IO, two case studies are carried out. In these case studies, it is investigated if DFT can be used to compare the opto-electrical properties of different doping types and -ratios. This is done for post-transition metals (Sn), transition metals (W and Mo) and anionic doping (F). By observing the partial density of states of each element, it was found that significant hybridization of dopant states with the CBM of the IO host states occurs for the cases of Sn- and F-doping. Such disturbance in the host conduction band may lead to detrimental influences to the opto-electrical properties of corresponding TCOs. However, in the cases of W- and Mo-doped TCOs at commonly used doping concentrations, no hybridization between dopant states and the host conduction band was observed. Furthermore, physical parameters of different TCOs at different doping levels are extracted and compared, such as band gap, effective electron mass, work function and dielectric functions. These results may provide supportive and indicative information for the experimental work.

This thesis work has successfully introduced DFT calculation into TCO investigations within our research group. Although the preliminary results were not sufficiently accurate to predict the opto-electrical properties of the TCOs in a quantitative way, the qualitative trend can still be used as guidance and support for explaining experimental results. However, many challenges still remain, especially for determining some optical properties like the band gap and dielectric function. Further research is still needed to improve the proposed method.

Acknowledgements

With this master thesis, my studies in Delft end after completing the *BSc Molecular Science & Technology* and the *MSc Sustainable Energy Technology*. After spending 7 years with many unforgettable experiences in this city, the time has come to start a new chapter in my career.

I would like to thank my daily supervisors Can Han and Dr. Rudi Santbergen. Even though all of our communication in the process has been online because of the pandemic, meetings were smooth and I felt like I could always approach the both of them. I would also like to thank Jouke Heringa and Antoon Frehe, as without them I would never have been able to perform the simulations on the server, as well as Alba Alcañiz Moya, who introduced me to the *VASP* software. Besides, I'm grateful for the *AMS* support crew, who where always reacting adequately when I would face obstacles with their software. I would also like to thank Dr. Olindo Isabella and Prof. Dr. Ferdinand Grozema for being part of my thesis committee.

Last but not least, I would like to thank my family, friends, roommates (both in Delft and Rotterdam) and Puck. Their support helped me to clear my mind when I needed it and kept me motivated.

Max van Duffelen
Rotterdam, July 2021

Contents

Abstract **iii**

Acknowledgements **v**

Nomenclature **ix**

List of Figures **xi**

List of Tables **xiii**

1 Introduction **1**
- 1.1 Solar Cells 1
- 1.2 TCOs 2
  - 1.2.1 Function 2
  - 1.2.2 Important Parameters 3
  - 1.2.3 Current Process. 3
- 1.3 PV Modelling 3
- 1.4 Ab initio modelling 4
  - 1.4.1 DFT on TCO materials. 5
- 1.5 Goals 5
- 1.6 Outline 5

2 Density Functional Theory & Implementation **7**
- 2.1 DFT Fundamentals. 7
  - 2.1.1 Schrödinger Equations 7
  - 2.1.2 The Born-Oppenheimer Approximation. 7
  - 2.1.3 The Hohenberg-Kohn Theorem. 8
  - 2.1.4 The Kohn-Sham Method 8
- 2.2 Iterative Process Scheme 9
- 2.3 Methods 9
  - 2.3.1 PAW method in *VASP* 9
  - 2.3.2 Slater Type Orbitals in *AMS* 10
- 2.4 Parameter Settings 10
  - 2.4.1 Exchange-Correlation Functionals 10
  - 2.4.2 K-points 11
  - 2.4.3 Cut-Off Energy 12
  - 2.4.4 Basis Sets 12
- 2.5 Extracting Relevant Properties 12
  - 2.5.1 Work Function 12
  - 2.5.2 Optical: Complex Refractive Index. 12
  - 2.5.3 Electrical: effective electron mass 14
- 2.6 Conclusions 15

3 Modelling Framework & Validation **17**
- 3.1 Structure: Crystallography 17
  - 3.1.1 Wyckoff sites 17
  - 3.1.2 Unit cell 17
- 3.2 Simulation Procedure 18
  - 3.2.1 *AMS* Benchmarking 18
  - 3.2.2 *VASP* Procedure 21

3.3 Validation . . . 23
3.3.1 Density of States . . . 23
3.3.2 Band Structure . . . 24
3.3.3 Work Function . . . 24
3.3.4 Complex Refractive Index . . . 25
3.4 Conclusions . . . 26

4 Case Study: IO with different dopants 27
4.1 Doping Site Preference. . . . 27
4.2 Band Structure and DOS . . . 28
4.3 Hybrid XC functional: DOS. . . . 30
4.4 Work Function . . . 31
4.5 Complex Refractive Index . . . 32
4.6 Conclusions . . . 33

5 Case Study: TCOs with varied doping ratios 35
5.1 Indium Tin Oxide (ITO) . . . 35
5.2 Indium Tungsten Oxide (IWO) . . . 37
5.3 Indium Fluorine Oxide (IFO) . . . 38
5.4 Overview . . . 40
5.5 Conclusions . . . 40

6 Conclusions & Recommendations 41
6.1 Recommendations . . . 42

Bibliography 45

Nomenclature

ϵ_x	Dielectric function
$\hat{H}$	Hamiltonian operator
$\hat{T}$	Kinetic operator
$\hat{U}$	Electron repulsion operator
$\hat{V}$	Potential operator
$\hbar$	Reduced Planck constant
μ	Electron mobility
ω_{ps}	Screened plasma frequency
ϕ_i	Molecular orbital
Ψ	System wave function
τ_c	Carrier relaxation time
E_0	Ground state energy
E_f	Fermi energy
E_{cut}	Cut-off energy
$E_{g,x}^{y}$	Band gap energy of compound *x*, using XC functional *y*
E_H	Hartree energy functional
E_{vac}	Vacuum energy
E_{VB}	Valence band energy
E_{xc}	Exchange-correlation functional
IE	Ionization energy
k	Extinction coefficient
m_e^*	Effective electron mass
m_e^0	Electron rest mass
n	Refractive index
N_e	Free carrier density
AMS	Amsterdam Modelling Suite
c-Si	Crystalline silicon
CBM	Conduction band minimum
DFT	Density functional theory
DOS	Density of states

F	Fluorine
FCA	Free-carrier absorption
GGA	Generalised gradient approximation
GTO	Gaussian-type orbitals
IFO	Indium fluorine oxide
IMO	Indium molybdenum oxide
In	Indium
IO/In_2O_3	Indium oxide
ITO	Indium tin oxide
IWO	Indium tungsten oxide
LCAO	Linear combination of atomic orbital
LDA	Local density approximation
MO	Molecular orbital
Mo	Molybdenum
O	Oxygen
PBE	Perdew, Burke and Ernzerhof
pDOS	Partial density of states
PHS	PBE + HSE06 + Sum rule
PV	Photovoltaic
PW91	Perdew-Wang 91
Sn	Tin
STO	Slater-type orbital
TCAD	Technology Computer Aided Design
TCO	Heyd, Scuseria and Ernzerhof
TCO	Transparent conducting oxide
VASP	Vienna *ab initio* Simulation Package
VBM	Valence band maximum
W	Tungsten
ZORA	Zeroth-order regular approximation

List of Figures

1.1 HJ c-Si solar cell 1
1.2 Solar cell with TCO 2
1.3 Burstein-Moss Shift 3
1.4 TCO fabrication & characterization process 4
1.5 Multi-scale modelling 4

2.1 Iterative scheme Kohn-Sham equations 10
2.2 Hierarchy ladder of XC functionals 11
2.3 Intrinsic semiconductor band structure 13

3.1 Conventional unit cell IO 18
3.2 In-8*b*, In-24*d* and O-48*e* Wyckoff site structures 18
3.3 Primitive unit cell IO 20
3.4 Brillouin Zone IO 22
3.5 *PBE* and *HSE06*-simulated DOS IO 23
3.6 *PBE*-simulated band structure, DOS and pDOS of IO 24
3.7 *PBE*-simulated local Potential IO 25
3.8 Simulated complex refractive index IO 25

4.1 *PBE*-simulated band structure, DOS & pDOS for ITO, IMO, IWO & IFO 28
4.2 *HSE06*-simulated DOS for IO, ITO, IWO & IFO 30
4.3 *PBE*-simulated local potential of IO, ITO, IMO, IWO and IFO 31
4.4 *PBE*-simulated complex refractive index of ITO, IMO, IWO & IFO 32

5.1 *HSE06*-simulated DOS of ITO 35
5.2 *PBE*-simulated band structure, DOS & pDOS for ITO, varied doping ratios 36
5.3 *PBE*-simulated band structure, DOS and pDOS of IWO, varied ratios 37
5.4 DOS of IWO, *HSE06* XC functional 38
5.5 *PBE*-simulated bandstructure and (p)DOS of IFO, varied ratios 38
5.6 *PBE*-simulated pDOS of IFO, varied ratios 39
5.7 Unit cell volume, band gap & m_e^* overview 40

List of Tables

3.1 Conventional IO basis set and XC functional determination for *AMS* 19
3.2 Primitive IO basis set and XC functional determination for *AMS* 20

4.1 Preferable doping site ITO, IMO and IWO 27
4.2 Ionization Energy Results 31
4.3 Chapter results summary 33

5.1 ITO with varied doping ratios 36
5.2 IWO with varied doping ratios 38
5.3 IFO with varied doping ratios 39

1
Introduction

1.1. Solar Cells

The direct conversion of solar energy into electricity is called the photovoltaic effect. It was observed for the first time in 1839 by French physicist Alexander Edmond Becquerel[1]. More than a century later, in 1954, the first practical solar cell made of crystalline silicon (c-Si) was invented at Bell Labs, USA[2]. Following this discovery The New York Times forecasts that solar cells will eventually lead to a source of ”limitless energy of the sun”. Even today, more than 95% of photovoltaics production is based on c-Si[3].

Ever since the first c-Si solar cell was invented the efficiency is improving step-by-step[4]. The very first silicon cells, as described in 1941, had an efficiency of only 1%[5]. Major improvements, such as the introduction of diffused junctions in 1954[2] and surface texturing in 1974[6] helped to reach an efficiency above 15%. Further improvements were obtained through surface passivation, bulk lifetimes, contact passivation and light trapping, which helped to reach the milestone efficiency of 25%[4]. Currently, the efficiency record of c-Si solar cells is 26.6%[7]. This is nearing the intrinsic efficiency limit of 29% for c-Si solar cells[8].

A c-Si solar cell is a thin device, consisting of several layers[8]. This is visualized in Figure 1.1, which shows the schematic of a c-Si solar cell with a very high efficiency of 25.1%[9]. A visualization of the different layers of a HJ c-Si solar cell is shown in Figure 1.1. The absorber layer is made of n-type Czochralski c-Si with a thickness of 200μm, with front-passivation done by a p$^+$ a-Si:H layer and back-passivation by a n$^+$ a-Si:H layer. Both the rear and front side of the solar cell have TCOs deposited and contain silver front and rear contacts. Layers may be textured to minimize reflection loss and enhance light trapping[10].

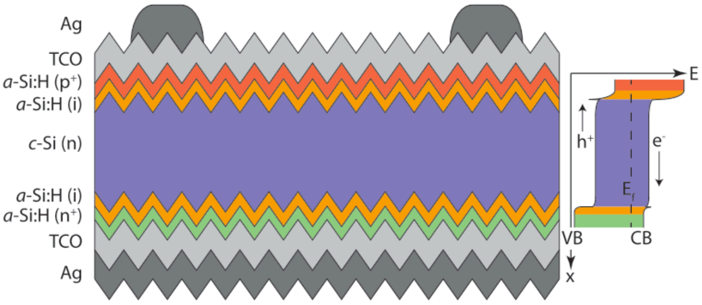

Figure 1.1: Schematic of a heterojunction crystalline silicon solar cell[10].

The working principle of a solar cell, the photovoltaic effect, can be described by three basic processes: generation, separation and collection of photo-generated charge carriers due to absorption of photons in a semiconductor material[11]. Negatively charged electrons and positively charged holes are separated and collected through front and back electrical contact. The back contact usually covers the entire back surface of the solar cell, as no light should be transmitted through the back. Instead, there is often a reflective layer present to extend the optical path of the light and with it the chance to be absorbed in the active layer[12]. For the front contact however, shading loss needs to be avoided to maximize photon transmission towards the absorber layer. This can be seen in Figure 1.1, as the silver front contact only covers a small part of the surface. Hence, a highly transparent layer with good electrical conductivity is required to provide lateral charge transport towards the metal front contact.

1.2. TCOs

Transparent conducting oxides (TCOs) exhibit the above mentioned characteristics of high transparency and good electrical conductivity. These transparent electrodes are a necessary component in many modern devices such as touch screens, LCDs, OLEDs and solar cells[13]. There exist many types of TCOs and for each application other types work optimally. Globally, the TCO market has an annual growth rate exceeding 17% and it is expected to have a market value of $8.46 billion by 2026[14]. Part of this high growth rate is due to the rising demand of solar cells. As of today, the global standard for TCOs is indium tin-oxide (ITO), accounting for 60% of the transparent conductor market as well as 60% of the indium market[15]. Due to indium being a relatively rare earth element and the rising demand, its prices can be extremely volatile. Because of this a lot of research has been done in discovering indium-free TCOs, although so far they have failed to reach ITO's performance[16–18].

1.2.1. Function

The requirements of TCO characteristics depend on the application it is being used for. The scope of this thesis is on TCOs for solar cell front contacts and therefore they will be discussed more in depth. In solar cells, TCOs are at the very front of the device as shown in Figure 1.2, although in some cases covered by a glass plate for protection against the outside environment. When a photon is incident on the TCO surface, it can either be reflected, absorbed or transmitted. Reflected and absorbed photons cause a loss in cell efficiency due to reflection- and parasitic absorption losses and should thus be minimized. There are several ways to minimize surface reflection. Adding surface texture and an anti-reflective coating are among them. Another method concerning TCOs especially, is to limit the screened plasma frequency (ω_{ps}) of the material. For photons with a frequency below ω_{ps} transmission decreases, as part of it will be strongly reflected[19].

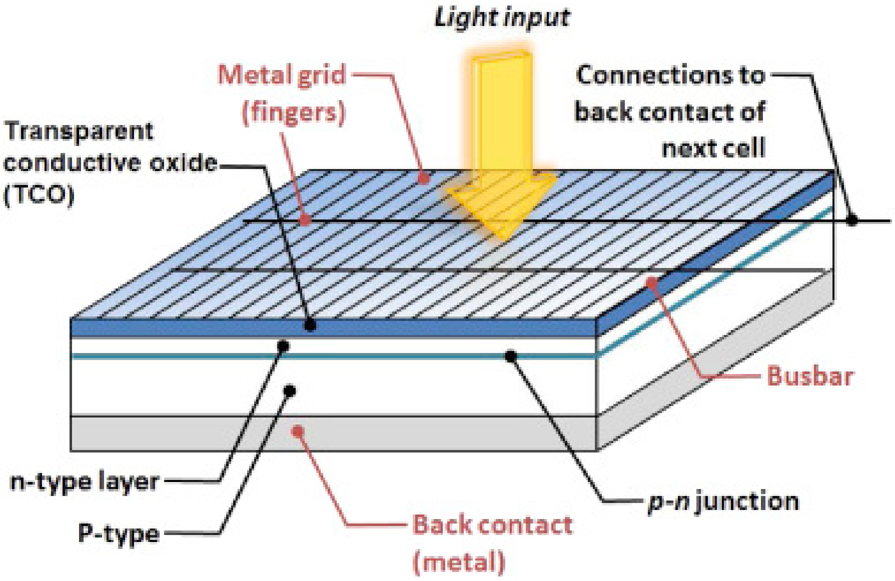

Figure 1.2: Schematic of a solar cell with a front TCO[20].

In semiconductors light can be absorbed if the photon energy is higher than the band gap of the material. Therefore, a requirement for TCOs in solar cells is to have a high band gap, so that most light is transmitted. Widening the band gap of a TCO greater than 3.1 eV permits transparency to most of the visible portion of the light spectrum. The host metal oxide in ITO, In_2O_3, has a wide band gap around 3.1 eV[21]. With such a high band gap it insulating, as the probability of exciting an electron into conduction is very low. To make the system conducting, electrons can be injected from a nearby defect donor level directly into the conduction band. This is done by degenerate doping of the host metal oxide, tin in case of ITO. This causes the Fermi level to shift above the conduction band minimum, which leads to an effect called the Moss-Burstein shift[22]: the apparent, optical band gap is increased with the difference between Fermi energy and conduction band minimum (Figure 1.3). In this thesis, the band structures of different TCOs obtained from DFT simulation will be explored, from which the opto-electrical properties will tentatively be predicted.

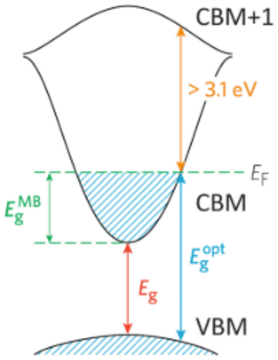

Figure 1.3: Illustration of the optical widening effect of the Burstein-Moss shift[23].

1.2.2. Important Parameters

The electrical conductivity of TCOs is proportional to the electron mobility (μ) and the free-carrier density (N_e)[24]. N_e is increased with degenerate doping of the host, shifting the Fermi level more above the conduction band minimum, thus making the system more conduction. However, and increase in N_e also leads to parasitic free carrier absorption (FCA) in the conduction band, a phenomenon well described by the classical Drude theory[25, 26]. Thus, increasing N_e leads to a higher conductivity and decreases transparency. Therefore, a trade-off has to be made between optical and electrical losses when selecting the optimum TCO.

The focus of this thesis is on n-type TCOs with the general formula M_xO_y:D, where M_xO_y is the host metal oxide and D the dopant element. Mainly, the host metal in n-type TCOs have the $(n - 1)d^{10}ns$ electronic configuration[27]. Indium is among the metals with this configuration and has proven to be a promising host material for producing TCOs with high electron mobility, thus will form the base of all TCOs covered in this thesis.

1.2.3. Current Process

The Photovoltaic Materials and Devices (PVMD) group at Delft University of Technology have developed opto-electrical models that allow for fast solar cell optimization. The Advanced Semiconductor Analysis Software (ASA) is designed for this and requires accurate and self-consistent opto-electrical properties of all layers as input. As of now, these properties are determined by doing measurements, which are often time consuming. Besides, it is difficult to carry out simulations with novel materials that are yet to be produced, as their opto-electrical properties are unknown. Characterization of TCOs is done as follows. First, the TCO is deposited on a glass substrate through RF magnetron sputtering[28]. In the R&D phase it is not necessary to do this on a silicon wafer yet, as the opto-electrical parameters can be determined from measuring at the glass substrate. Optical properties are then obtained through ellipsometry and UV-Vis-NIR measurements. Electrical properties are obtained using the four-point probe method and Hall measurements.

1.3. PV Modelling

Before constructing a PV system at a certain location, PV modelling is a vital part of the implementation phase[29]. The *Photo Voltaic Materials & Devices* (PVMD) group of the department *Electrical Sustainable Energy* covers many disciplines corresponding to solar energy, including PV modelling.

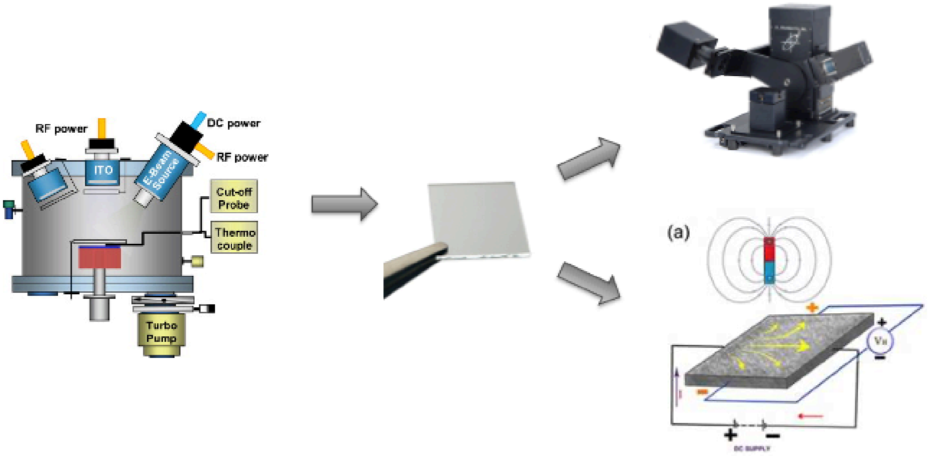

Figure 1.4: Illustration of the current process of TCO fabrication and characterization.

The discipline of PV modelling covers any scale possible. On the largest scale, modelling the location of a PV system is crucial in determining the orientation of modules and to optimize the sizing. Irradiance, cloud coverage and temperature are among the inputs needed for this type of modelling. With respect to the module, one needs to know its efficiency an maximum power output. These can be obtained through modelling at the PV module scale, which uses input as the cell *JV*-curve to construct the module *JV*-curve. The cell *JV*-curve can in turn be obtained by modelling at the cell level, through softwares like TCAD Sentaurus[30] and ASA[31]. These softwares allow for fast solar cell optimization, but do require accurate and self-consistent opto-electrical material properties of each solar cell layer as input. One of the layers of which these properties need to be determined, is the TCO.

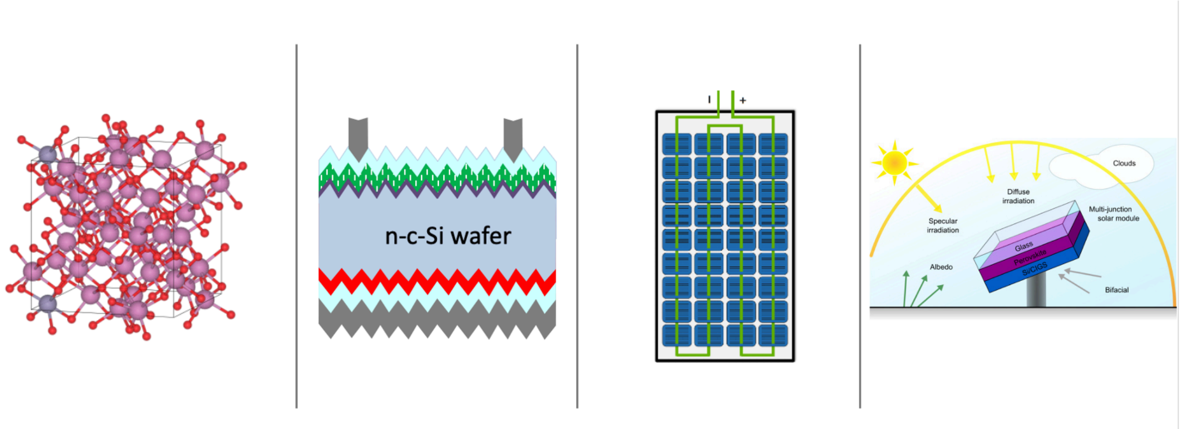

Figure 1.5: Illustration of the various scales of PV modelling. From left to right: Atomistic modelling, cell modelling, module modelling and system modelling

1.4. Ab initio modelling

Another approach to obtain the opto-electrical properties is by simulation. Density functional theory (DFT) is a computational quantum mechanical modelling method that investigates the electronic structure of many-body systems, using only the atomic structure as input[32]. DFT software then solves the system as a set of n one-electron Shrödinger equations. As quantum mechanics states that the majority of information we can possibly have about a given system is described in the systems wave functions. Thus, in principle, it is possible to obtain all material properties[33]. To understand how *ab initio* modelling can be used to obtain these properties, an in-depth explanation will be given in Chapter 2. In a nut-shell, density functional theory reduces a 3N-dimensional problem to a 3-dimensional one using approximations in order to reduce computational computing power. Unlike many other software, DFT is not a ”black box” which converts inputs into usable results. Instead, simulation settings must be defined carefully to achieve results that are referable to experimental results.

1.4.1. DFT on TCO materials

DFT software has been used for atomistic modelling of TCOs. Most of these studies have been done on ITO[34–36]. Recently, there also has been some development recently in the field of IMO, where it was claimed that Molybdenum clearly outperforms Tin as a dopant[15]. The methods described in this literature serve as a starting point for the modelling framework set in this thesis. This method will then be used for similar simulations on ITO and IMO, with differing dopant ratios.
At the PVMD group, research is being done on the relatively new TCO materials of IFO and IWO[37, 38]. In this work, preliminary simulated results are obtained, which could be referable to experimental results. It will be investigated if the measured results can be replicated by DFT simulations.

1.5. Goals

There are three goals in this thesis:

- *Ab initio* modelling is relatively new to the PVMD group, with the AMS software yet to be introduced and the VASP software being used only once before to our knowledge[39]. Therefore, the first goal is to gain experience in this field and set the modelling framework. This knowledge will then be shared within the PVMD group for further research.
- The second goal is to compare computational methods and select the best simulation settings to obtain reliable results. The method will be validated using the TCO host, indium-oxide.
- The third goal is to do a case study to investigate the opto-electrical properties of different IO TCO materials. For this, different input parameters of the material, like dopant ratio and dopant site, will be adjusted. Here, it will be investigated if qualitative and/or quantitative agreement with experiments can be obtained.

In order to reach above mentioned goals, the following research questions will be answered in this thesis:

1. How does DFT software solve the Schrödinger equation?
2. With what calculation settings does DFT software provide results comparable to experiment, using the TCO host indium oxide?
3. Can DFT be used to qualitatively or quantitatively examine the opto-electrical parameters of different IO-doped TCOs?
4. Can DFT be used to qualitatively or quantitatively analyse the effect of dopant ratio on IO-doped TCOs?

1.6. Outline

In Chapter 2 some background information, theory and implementation of density-functional theory will be given, answering the first research question. Next, in Chapter 3, the indiumoxide structure is introduced, as well as the calculation settings to obtain reliable results, thus answering the second research question. This forms the base of the simulations performed in Chapters 4 and 5, answering the third and fourth research questions. The thesis finalizes with conclusions and recommendations for further research in Chapter 6.

2

Density Functional Theory & Implementation

As mentioned in Chapter 1, density-functional theory is a computational method that iteratively approximates the solution to the Schrödinger equation. The main goal of this chapter is to find out which opto-electrical properties can be obtained through DFT. To reach this goal, a more in-depth understanding of DFT and its fundamental principles is needed. This chapter is structured as follows. Section 2.1 explains the fundamentals of DFT, after which the computational implementation is presented in section 2.2. Next, section 2.3 describes briefly how the two used softwares, *VASP* and *AMS*, implement DFT. Section 2.4 gives an overview of the input parameters of each software. Finally, section 2.5 gives an explanation on how to extract relevant material properties from DFT calculations. Here, also the limitations of DFT on extracting material properties will be given.
At the end of this chapter, the reader should be able to understand the physical principles underlying DFT and how it can be used to extract relevant material properties, as well as its limitations.

2.1. DFT Fundamentals

Density-functional theory (DFT) is a computational quantum mechanical modelling method. Its purpose is to investigate the electronic structure of many-body systems [40]. It is an *ab initio* modelling method, meaning literally ”from the start”. This means that the input for this method is the smallest input possible: the atomistic structure. Higher-order parameters are not required.

2.1.1. Schrödinger Equations

Quantum mechanics state that all information we can possibly have about a given system is described in the systems wave function, Ψ[33], which is part of the time-dependent Schrödinger equation:

$$i\hbar\frac{\partial}{\partial t}|\psi(t)\rangle = \hat{H}|\psi(t)\rangle \tag{2.1}$$

Where $i = \sqrt{-1}$ is the imaginary unit, $\hbar$ the reduced Planck constant, $\hat{H}$ is the Hamiltonian operator and ψ is the wave function. ψ descirbes the many-body problem as a system of electrons with positions $\vec{r}_\mathrm{n}$ and ions, the nuclei, with positions $\vec{R}_\mathrm{n}$, notated as: $\phi = \phi\left(\vec{r}_1, \vec{r}_2, \ldots; \vec{R}_1, \vec{R}_2, \ldots; t\right) = \phi(\vec{r}, \vec{R}; t)$.

The Hamiltonian operator ($\hat{H}$) is the sommation of the kinetic operator ($\hat{T}$) and potential operator ($\hat{V}$). Both operators consist of nuclear (R) and electronic (r) terms. The potential operator ($\hat{V}$) also consists of a mixed term (r, R). The Hamiltonian operator can thus be redefined as:

$$\hat{H} = \hat{T}_R + \hat{T}_r + \hat{V}_R + \hat{V}_r + \hat{V}_{r,R} \tag{2.2}$$

As the solution to the Schrödinger equation is only exactly solvable for the smallest systems, e.g. a hydrogen molecule, solutions for complex systems, like solids, need to be approximated.

2.1.2. The Born-Oppenheimer Approximation

The Born-Oppenheimer approximation is an assumption that the wave functions of atomic nuclei and electrons of a molecule can be treated seperately, as the nuclei are much heavier than the electrons[41]. Given the same kinetic energy, the nuclei move much slower than the electrons and thus are approximated to be static from the electrons' point of view. This results in the wavefunction of a molecule to be the product of the electronic- and nuclear wavefunction, enabling separation of the Hamiltonian operator into electronic and nuclear terms. The mixed term of the potential operator ($\hat{V}_{r,R}$) is neglected.

The wave function depends only on the electronic coordinates, as the nuclear degrees of freedom appear in the form of a static external potential V acting on the electrons according to the Born-Oppenheimer approximation[41]. Then, the many-electron time-independent Schrödinger equation is given by:

$$\hat{H}\Psi = [\hat{T} + \hat{V} + \hat{U}]\Psi = \left[\sum_{i=1}^{N}\left(-\frac{\hbar^2}{2m_i}\nabla_i^2\right) + \sum_{i=1}^{N} V(\mathbf{r}_i) + \sum_{i<j}^{N} U(\mathbf{r}_i, \mathbf{r}_j)\right]\Psi = E\Psi \tag{2.3}$$

Here, $\hat{V}$ represents the nuclei-electron attraction and $\hat{U}$ the electron-electron repulsion. The first term is $\hat{T}$ is the kinetic operator.

The ground-state energy E_0 can be obtained by minimization of the Hamiltonian according to the variational theorem[42]:

$$E_0 = \min_{\Psi}\langle\Psi|\hat{H}|\Psi\rangle \tag{2.4}$$

As the energy can never be lower than the ground-state energy, the calculation that results in the lowest energy is the one closest to the ground state. Therefore, even without knowing the exact ground-state energy, one can still say that the calculation resulting in the lowest energy is the most accurate. This is important to realize when comparing different calculations, which will be further discussed in Section 2.4.

DFT is based on a reformulation of above mentioned minimization, in terms of the one-electron density:

$$n(\mathbf{r}) = N\int\cdots\int |\Psi(\mathbf{x}, \mathbf{x}_2, \ldots, \mathbf{x}_N)|^2 \; \mathrm{d}\sigma \mathrm{d}\mathbf{x}_2 \ldots \mathrm{d}\mathbf{x}_N \tag{2.5}$$

Where σ is the spin coordinate, which is either up or down.

2.1.3. The Hohenberg-Kohn Theorem

The Hohenberg-Kohn theorem[43] states that there is one-to-one mapping of the ground state density to the potential. Hence, the ground-state density determines the potential, which in turn determines the Hamiltonian. The potential is therefore a unique functional of all properties of the many-body system[42]. The universal density functional is:

$$F[n] = \langle\Psi[n]\,|\hat{T} + \hat{W}_{\mathrm{ee}}|\,\Psi[n]\rangle \tag{2.6}$$

Together with the specific external potential v_{ne} it gives the total electronic energy functional:

$$E[n] = F[n] + \int v_{\mathrm{ne}}(\mathbf{r})n(\mathbf{r})\mathrm{d}\mathbf{r} \tag{2.7}$$

2.1.4. The Kohn-Sham Method

A minimization of this electronic energy functional returns the ground-state energy E_0, which is reached for a ground-state density n_0. However, the exact expression of $F[n]$ in terms of density is unknown, therefore it is difficult to approximate $F[n]$ directly. Kohn and Sham (KS)[44] proposed a method to decompose $F[n]$ in the non-interacting kinetic-energy functional $T_s[n]$ and the Hartree-exchange-correlation-functional $E_{\mathrm{Hxc}}[n]$. This allows for the ground-state energy to be written in *single-determinant* wave-functions only, of which the derivation can be found in [42]:

$$E_0 = \min_{\Phi}\left\{\langle\Phi\,|\hat{T} + \hat{V}_{\mathrm{ne}}|\,\Phi\rangle + E_{\mathrm{Hxc}}[n_\Phi]\right\} \tag{2.8}$$

Now, only $E_{\mathrm{Hxc}}[n]$ needs to be approximated as a functional of the density:

$$E_{\mathrm{Hxc}}[n] = E_{\mathrm{H}}[n] + E_{\mathrm{xc}}[n] \tag{2.9}$$

Where the Hartree energy functional is given by:

$$E_{\mathrm{H}}[n] = \frac{1}{2} \iint \frac{n(\mathbf{r}_1)\, n(\mathbf{r}_2)}{|\mathbf{r}_1 - \mathbf{r}_2|} \mathrm{d}\mathbf{r}_1\, \mathrm{d}\mathbf{r}_2 \tag{2.10}$$

The exchange-correlation functional $E_{\mathrm{xc}}[n]$ remains approximate. There are many models that approximate the exchange-correlation energy, from simple to very sophisticated, which have been described in depth in [45]. The exchange-correlation functionals that will be used in this thesis will be introduced in subsection 2.4.1.

In KS decomposition, the total energy of a many-electron system in an external potential is given by[40]:

$$E[n] = T_0[n(r)] + \int drn(r)v_{\mathrm{ext}}(r) + E_H[n(r)] + E_{xc}(r) \tag{2.11}$$

This equation consists of the kinetic energy:

$$n(r) = \sum_{i}^{\mathrm{occ}} |\psi_i(r)|^2 \tag{2.12}$$

the external potential from the nuclei:

$$v_{\mathrm{ext}} = -\sum_{n} \frac{Z_n}{r - R_I} \tag{2.13}$$

the classical Coulomb energy:

$$E_{\mathrm{H}}[n] = \frac{1}{2} \iint \frac{n(\mathbf{r}_1)\, n(\mathbf{r}_2)}{|\mathbf{r}_1 - \mathbf{r}_2|} \mathrm{d}\mathbf{r}_1\, \mathrm{d}\mathbf{r}_2 \tag{2.14}$$

and finally, the exchange and correlation:

$$E_{xc}[n] = \int drn(r)\varepsilon_{xc}[n(r)] \tag{2.15}$$

This KS decomposition separates contributions to the total energy that are, in principle, possible to compute from contributions that are much more complicated, like the exchange-correlation.

2.2. Iterative Process Scheme

DFT softwares solve the Kohn-Sham equations iteratively. This works as follows. First, an initial guess given, which is usually a superposition of atomic densities for $k = 1$. Then, the effective potential is evaluated after which the Kohn-Sham equations are solved for this potential. Then, the actual density is evaluated. If the cycle is consistent with the set accuracy, the external parameters can be extracted from the wave function. If not, another iteration is needed. See Figure 2.1 for a schematic of the self-consistency loop[40].

2.3. Methods

Several softwares exist for *ab initio* modelling, of which two are used in this thesis: the Vienna Ab initio Simulation Package (*VASP*)[46–49] and the Amsterdam Modelling Suite (*AMS*)[50]. Although both softwares approximate the Schrödinger equations iteratively, their working principle is slightly different. This section briefly covers the principles behind *VASP* and *AMS*.

2.3.1. PAW method in *VASP*

The projector augmented wave (PAW) method is a generalization of the pseudopotential- and linear augmented-plane-wave methods. It allows for DFT calculations with greater computational efficiency[51]. The use of pseudopotentials, in which the collective system of nuclei and core electrons are described by an effective, much smoother, potential, reduces the size of the plane wave set for a DFT calculation

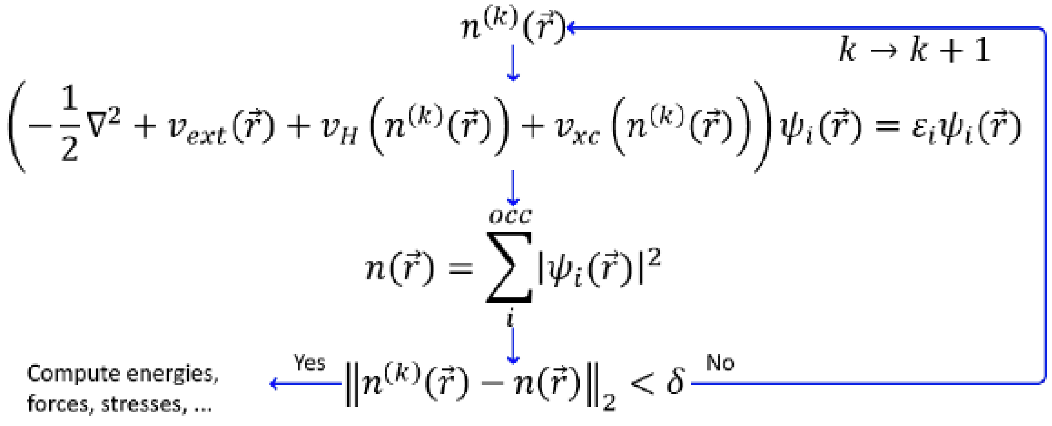
$n^{(k)}(\vec{r})$
$k \rightarrow k+1$
$\left(-\frac{1}{2}\nabla^2 + v_{ext}(\vec{r}) + v_H\left(n^{(k)}(\vec{r})\right) + v_{xc}\left(n^{(k)}(\vec{r})\right)\right)\psi_i(\vec{r}) = \varepsilon_i\psi_i(\vec{r})$
$n(\vec{r}) = \sum_i^{occ} |\psi_i(\vec{r})|^2$
Compute energies, forces, stresses, ...
Yes
$\left\|n^{(k)}(\vec{r}) - n(\vec{r})\right\|_2 < \delta$
No

Figure 2.1: Iterative Process Scheme of the solution of the Kohn-Sham equations[39].

significantly[52]. The pseudopotentials of nuclei and core electrons are calculated and tabulated once for each atom and usually provided with the license of DFT software. Now, the solution can be obtained by calculation of the valence states only. Further explanation can be found in [49, 51–53]. *VASP* is among the softwares using the PAW-method[46–48].

2.3.2. Slater Type Orbitals in *AMS*

AMS has a different approach in approaching the solution to the Schrödinger equation, as it uses slater-type orbitals (STOs). These orbitals are functions used as atomic orbitals in the linear combination of atomic orbital (LCAO) method[54]. This can be expressed by the following equation:

$$\phi_i = \sum_r c_{ri}\chi_r \tag{2.16}$$

Where ϕ_i is a molecular orbital that is represented as the sum of n atomic orbitals χ_r, multiplied by a corresponding coefficient c_{ri}. A qualitative treatment of LCAO is provided by using MO diagrams.
The advantage of STOs over Gaussian-type functions (GTOs) is that often a smaller number of STOs is needed to obtain the same accuracy[55].

2.4. Parameter Settings

In this section, a number of parameters that are used as input in DFT software are presented. It is important to realize that selecting certain parameters strongly influence the calculation accuracy and inversely the computational speed.

2.4.1. Exchange-Correlation Functionals

The part of DFT calculation that is 'impossible' to solve, is the exchange-correlation energy potential, E_{xc}. An assumption is made to approximate the value of E_{xc} by selection an exchange-correlation functional. There are several approximations possible, and selecting the best XC-functional depends on the intend of the DFT calculation, as well as the accuracy and computational power available. Part of the available XC-functionals is summarized in Figure 2.2.

LDA

The simplest XC functional, is the local density approximation (LDA). As LDA only depends on one variable, the density, it is considered to be not accurate enough for many purposes.

$$E_{xc}^{LDA}[n(r)] = \int n(r)\varepsilon_{xc}^{\text{hom}}[n(r)]dr \tag{2.17}$$

PW91

The PW91 XC functional is a generalised gradient approximation (GGA), which contains the next term in a derivative expansion of the charge density and is therefore dependent on two variables: the electron

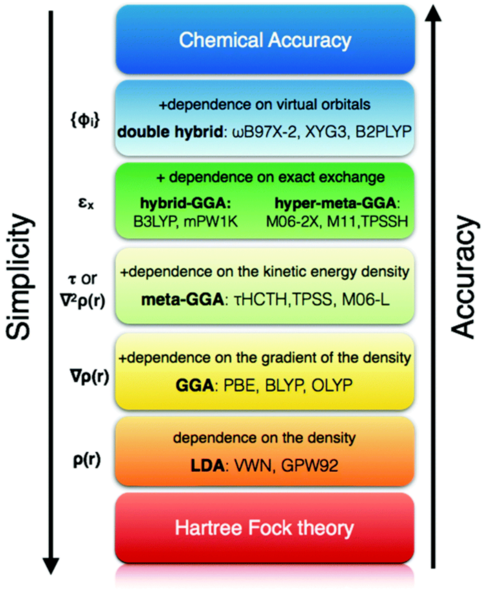
Chemical Accuracy
{ϕi}
+dependence on virtual orbitals
double hybrid: ωB97X-2, XYG3, B2PLYP
εx
+ dependence on exact exchange
hybrid-GGA: B3LYP, mPW1K
hyper-meta-GGA: M06-2X, M11,TPSSH
τ or ∇²ρ(r)
+dependence on the kinetic energy density
meta-GGA: τHCTH,TPSS, M06-L
∇ρ(r)
+dependence on the gradient of the density
GGA: PBE, BLYP, OLYP
ρ(r)
dependence on the density
LDA: VWN, GPW92
Hartree Fock theory
Simplicity
Accuracy

Figure 2.2: Jacob's Hierarchy Ladder of Exchange-Correlation functionals[56].

density and its gradient[57]. This XC functional has previously been used to examine ITO through DFT software[34].

$$E_{xc}^{GGA}[n(r)] = \int n(r)\varepsilon_{xc}^{GGA}[n(r), \nabla n(r)]dr \tag{2.18}$$

PBE

The functional of Perdew, Burke and Ernzerhof (PBE) employs a semilocal approximation to the exchange-correlation energy[58]. The PBE XC functional is also a GGA and was based on its predecessor: the PW91 XC functional. The difference is that PBE ignores two features of PW91, which are described in [59]. The PBE XC functional is a popular choice for DFT calculations on TCOs [35][60][61].

$$E_{xc}^{GGA}[n(r)] = \int n(r)\varepsilon_{xc}^{GGA}[n(r), \nabla n(r)]dr \tag{2.19}$$

A shortcoming of these *GGA* functionals is the systematical underestimation of the band gap with respect to experiment[62, 63].

HSE06

An often used hybrid XC functional, is the one developped by Heyd, Scuseria and Ernzerhof: *HSE06*. It uses an error-function-screened Coulomb potential to calculate the exchange portion of the energy in order to improve computational efficiency[64]. The *HSE06* functional is often used for accurate band gap calculation of TCO materials, especially for ITO[61][60][65]. It was also used recently for DFT calculations on IMO[15].

$$E_{\mathrm{xc}}^{\omega\mathrm{PBEh}} = aE_{\mathrm{x}}^{\mathrm{HF,SR}}(\omega) + (1-a)E_{\mathrm{x}}^{\mathrm{PBE,SR}}(\omega) + E_{\mathrm{x}}^{\mathrm{PBE,LR}}(\omega) + E_{\mathrm{c}}^{\mathrm{PBE}} \tag{2.20}$$

2.4.2. K-points

A crystal is a highly ordered structure which can be described by a periodicity of unit cells[66]. Structures like these follow Bloch's theorem, which states that solutions to the Schrödinger equation in a periodic potential take the form of a plane wave modulated by a periodic function[67]. Therefore, the wave function in a crystal can be expressed as the product of a plane wave and a function:

$$\psi_i(\vec{r}) = e^{-i\vec{k}\vec{r}}u_i(\vec{r}) \tag{2.21}$$

Where $u_i(\vec{r})$ is periodic in real space: $u_i(\vec{r} = u_i(r + \vec{R}_{uvw})$[68]. These functions are called Bloch functions. The description of waves in a periodic medium can be completely characterized by their behaviour in a single Brillouin zone: a uniquely defined primitive cell in reciprocal space[69]. Reciprocal space, also k-space, is a way to visualize the results of the Fourier transform of a spatial function. The reciprocal space can be described by a discrete set of k-points.

There are several ways k-points can be specified, but unless stated differently, the k-points in this thesis is an automatically generated regular mesh of points. A larger number of k-points results in larger accuracy in DFT calculations, but also significantly increases the computational time.

2.4.3. Cut-Off Energy

As Bloch's theorem is obeyed and the Bloch functions are periodic, Equation 2.21 can be expanded by Fourier Expansion:

$$\psi_i(\vec{r}) = \sum_{\vec{G}} u_i(\vec{G}) e^{-i(\vec{G}+\vec{k})\vec{r}} \tag{2.22}$$

Which, in practice, is truncated to include all G for which:

$$\frac{\hbar}{2m}(\vec{G}+\vec{k})^2 < E_{cut} \tag{2.23}$$

Together with the k-points, E_{cut} is the most important parameter to check for convergence in the DFT iteration process as shown in Figure 2.1. A lower cut-off energy ultimately leads to higher accuracy.

2.4.4. Basis Sets

A basis set is a set of functions that is used to represent the electronic wave function in DFT. This enables the partial differential equations of the model to be turned into algebraic equations, which are suitable for efficient implementation on a computer.
AMS uses Slater-Type Basis Sets, which are optimized for the use in the zeroth-order regular approximated (ZORA) relativistic equation. This is reported to be an excellent approximation to the fully relativistic Dirac equation[55].

2.5. Extracting Relevant Properties

In this thesis, the ultimate goal for of the DFT calculations is to extract the opto-electrical properties. In this section, methods will be presented that are used in DFT software to extract these properties. In some cases, post-treatment of the DFT results is necessary to get the relevant properties.

2.5.1. Work Function

The work function is defined as the minimum energy that is required to remove an electron from a solid to a point in the vacuum[11]. In other words, the difference between the vacuum energy (E_{vac}) and the Fermi energy (E_{fermi}), as shown in Figure 2.3. The work function is a useful surface property that is often necessary as input for solar cell modelling software, like *TCAD Sentaurus*.
The input variable needed for *TCAD Sentaurus* is the valence band energy (E_{VB}) with respect to the vacuum energy (E_{vac}): the ionization energy (IE). As in *VASP* the Fermi energy is always set at 0 eV, the IE is simply extracted as: IE = $E_{VB} - E_{vac}$.

2.5.2. Optical: Complex Refractive Index

The optical property of interest is the complex refractive index, which is derived from the dielectric function. The dielectric function describes the dielectric response to the plane-wave electric field[71]. From the dielectric function, one can extract the complex refractive index, which in turn is used to extract reflectance and transmittance in cell-level modelling softwares like *ASA* and *TCAD Sentaurus*.

After the electronic ground-state has been determined by *VASP*, it calculates the dielectric matrix, consisting of a real and imaginary part. The imaginary part is determined by a summation over empty states[72]:

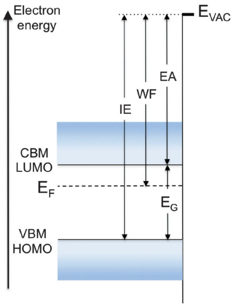

Figure 2.3: Visualization of the energy levels in an intrinsic semi-conductor[70].

$$\epsilon''_{\alpha\beta}(\omega) = \frac{4\pi^2 e^2}{\Omega} \operatorname{Lim}_{q\to 0} \frac{1}{q^2} \sum_{c,v,k} 2\omega_k \delta\left(\epsilon_{ck} - \epsilon_{vk} - \omega\right) \left\langle u_{ck+e_\alpha q} \mid u_{vk}\right\rangle \left\langle u_{ck+e_\beta q} \mid u_{vk}\right\rangle \tag{2.24}$$

The real part is obtained by Kramers-Kronig (KK) transformation[73]:

$$\epsilon'_{\alpha\beta}(\omega) = 1 + \frac{2}{\pi} P \int_0^\infty \frac{\epsilon''_{\alpha\beta}\left(\omega'\right)\omega'}{\omega'^2 - \omega^2 + i\eta} d\omega' \tag{2.25}$$

The complex refractive index is then obtained through[74, 75]:

$$n = \sqrt{\frac{|\varepsilon_r| + \varepsilon_{\mathrm{r}}}{2}} \tag{2.26}$$

$$\kappa = \sqrt{\frac{|\varepsilon_r| - \varepsilon_{\mathrm{r}}}{2}} \tag{2.27}$$

Where $|\varepsilon_r| = \sqrt{\varepsilon_{\mathrm{r}}^2 + \tilde{\varepsilon}_{\mathrm{r}}^2}$ is the complex modulus.

PHS-method

As DFT calculations are known to severely underestimate the bandgap of materials, the dielectric function is often shifted on the spectrum[76]. Fujiwara et al. developped a calculation procedure that obtained reliable results of the dielectric function in a consistent matter: the PBE + HSE06 + Sum rule (PHS) method. For that, a very high density k-mesh calculation using the PBE exchange-correlation functional, as well as accurate band gap determination using the hybrid *HSE06* functional was used. This method, which has been described in depth[76], will be used to post-treat DFT calculation results on the dielectric function. The real and imaginary parts of the dielectric function are obtained through the following formulas:

$$\varepsilon_{2,PHS}(E) = \frac{E - \Delta E_g}{E} \varepsilon_{2,PBE}\left(E - \Delta E_g\right) \tag{2.28}$$

$$\varepsilon_{1,\mathrm{PHS}}(E) = 1 + \frac{2}{\pi} P \int_0^\infty \frac{E' \varepsilon_{2,\mathrm{PHS}}\left(E'\right)}{E'^2 - E^2} dE'. \tag{2.29}$$

Where ΔE_g is the band gap difference between the HSE06 and PBE calculations.

The n and k values of the complex refractive index are determined by their conventional formulas:

$$n_{\mathrm{PHS}} = \left\{\left[\varepsilon_{1,\mathrm{PHS}} + \left(\varepsilon_{1,\mathrm{PHS}}^2 + \varepsilon_{2,\mathrm{PHS}}^2\right)^{1/2}\right]/2\right\}^{1/2} \tag{2.30}$$

$$k_{\mathrm{PHS}} = \left\{\left[-\varepsilon_{1,\mathrm{PHS}} + \left(\varepsilon_{1,\mathrm{PHS}}^2 + \varepsilon_{2,\mathrm{PHS}}^2\right)^{1/2}\right]/2\right\}^{1/2} \tag{2.31}$$

And finally, the absorption spectrum a of the PHS method is calculated through the conventional formula which is dependent on the extinction coefficient k: $\alpha_{\mathrm{PHS}} = 4\pi k_{\mathrm{PHS}}/\lambda$.

Band Gap

In order to minimize parasitic absorption, TCOs must be highly transparent in the spectral region where the solar cell is operating. This is in the UV-vis-NIR range, with wavelengths from 300-1200 nm[77]. Therefore, TCOs are semiconductors with a wide bandgap larger than 3.1 eV, corresponding to the photon energy of near-UV-light[16].

High transmittance is achieved by minimizing both absorptance and reflectance. To make a good comparison between TCOs, it is better to compare the parasitic absorptance, as it is easier to quantify independently of the substrate on which the TCO is deposited and the surface roughness[24]. The spectrally weighted absorptance, which is to be minimized, is given by Equation 2.32:

$$A_{\text{weighted },x} = \frac{\int_{\lambda_{1,x}}^{\lambda_{1,x}} I_{\text{light },x}(\lambda)A(\lambda)\mathrm{d}\lambda}{\int_{\lambda_1}^{\lambda_2} I_{\text{light },x}\ \mathrm{d}\lambda} \tag{2.32}$$

$A(\lambda)$ is the parasitic absorptance of the TCO as function of the wavelength. This absorption of free carriers is described by the classical Drude theory, stating that a higher free-carrier density (N_e) leads to higher free-carrier absorption[78].

The band gap can be obtained through DFT calculations by analyzing the band structure or the density of states (DOS), which describes the proportion of states that are to be occupied by the system at each energy[11]. The band gap can be seen as the size of the 'forbidden area' in the DOS: a state is not allowed to have an energy that lies within the band gap.

2.5.3. Electrical: effective electron mass

The electrical property that is to be optimized is the electrical conductivity: $\sigma = e\mu N_e$. σ is proportional to the electron mobility μ and the free-carrier density.

From the definitions of free-carrier absorption and electrical conductivity it becomes clear why a trade-off between optical and electrical losses has to be made. An increase in N_e leads to both higher conductivity and free-carrier absorptance, the latter lowering the transmittance of the TCO. Therefore, the best strategy for TCO optimization is to limit N_e and maximize electron mobility.

An electron's effective mass, m_e^* is the mass it *seems* to have when responding to forces. It is used to calculate the electrical conductivity of a material.

$$m_{eff}^{-1} = \hbar^{-2}\frac{\partial^2 E}{\partial k^2} \tag{2.33}$$

The effective electron mass can be obtained through *ab initio* calculation through fitting the curvature of the conduction band, i.e., the valley surrounding the Γ-point to the following equation[79]:

$$E(k) = E_o + \frac{h^2k^2}{8\pi^2 m^*} \tag{2.34}$$

Once the effective electron mass is determined, it can be used to obtain the electron mobility through: $\mu_e = \frac{e\tau_c}{m_e^*}$[11].

2.6. Conclusions

The goal of this chapter was to find out which opto-electrical properties of TCOs can, in principle, be extracted using DFT. To reach this goal, a good understanding of DFT and its working principle was necessary. We found out that there are different approaches in the DFT area, like the Slater-type orbital basis sets used in *AMS* and the pseudopotential approach used in *VASP*. Besides, it has become clear that simulation settings are crucial in DFT. There is always a trade-off between simulation accuracy and computational load. The different simulation settings will be investigated in Chapter 3, where the modelling method of this thesis will be given.

The band gap is an important property that can be extracted using DFT. However, from literature it is well known that the simulated band gap using DFT is severely underestimated for most XC functionals. Referable band gap simulations can be obtained by using the hybrid *HSE06* XC functional, but this comes at a very high computational cost. This is an important limitation of DFT, as the band gap is a fundamental property which is used to extract many more optical properties, like the dielectric function. The effective electron mass can be extracted from the simulated band structure. This property can then be used to calculate the electrical conductivity.

3

Modelling Framework & Validation

The first goal of this thesis was to understand the principles behind DFT softwares and how to extract relevant opto-electrical properties. This goal was reached by answering the first research question in Chapter 2. The goal of this chapter is to use this knowledge to answer the second research question: *with what calculation settings does DFT software provide results comparable to experiment?* Various computational methods will be compared to check if a quantitative or qualitative agreement with experimental data can be achieved using the TCO host, indium oxide.

This Chapter covers the validation of the method used to calculate the external parameters of TCOs using DFT. In Section 3.1 the structure of the TCO host, indium oxide (IO), will be explained. As was seen in Chapter 2, there are different methods possible to obtain the opto-electrical parametrs. These will be explored in Section 3.2, where different approaches regarding software used, structure input and chosen XC functional will be compared. Results of the IO-simulations will be presented and compared with experimental results in Section 3.3. This chapter closes with a conclusion, where the procedure for following simulations as presented in Chapter 4 will be summarized.
At the end of this chapter, the reader should understand what DFT simulation settings should be used to obtain reliable results.

3.1. Structure: Crystallography

The host material for most TCOs, indiumoxide, is a crystal, meaning it consists of a periodic arrangement of a unit cell into a lattice[66]. Indium (In) is a post-transition metal with an electron configuration of [Kr] $4d^{10}5s^{2}5p^{1}$. In the IO compound, In donates its three outermost 5s and 5p electrons to become indium(III). Oxygen (O) has the electron configuration of [He]$2s^{2}2p^{2}$ and an oxidation state of 2. Thus, an IO crystal has an In:O atomic ratio of 2:3 to become In_2O_3.

There are two ways in which IO can crystallize: the cubic (bixbyite type) and the rhombohedral (corundum type), the latter of the two existing after applying both high pressure and temperature[80]. The focus of this work will be the bixbyite structure, which contains 80 atoms in the conventional unit cell (Figure 3.1) and 40 atoms in the primitive unit cell[81].

3.1.1. Wyckoff sites

In the bixbyite structure of In_2O_3, there are two different indium-sites, each six-fold coordinated with oxygen-atoms: In-8*b*, which is highly symmetric, and In-24*d*, which is less symmetric[81]. A visualization is given in the first two structures of Figure 3.2. The numbers '8' and '24' is the multiplicity on the site, and indicates how many of these types there are present in the conventional unit cell. The letters *b* and *d* indicate the Wyckoff positions, which has no physical meaning, but are assigned alphabetically from the lowest multiplicity to the highest[66].
Each O-atom is four-fold coordinated, surrounded by In atoms, with a local structure of a distorted tetrahedron with all four In-O bonds inequivalent[81]. See the third structure of Figure 3.2 for a visualization.

3.1.2. Unit cell

The unit cell of a crystal is the smallest repeating unit having the full symmetry of the crystal structure[66]. As shown in Figure 3.1, the conventional, cubic unit cell of IO is rather large. IO also has a primitive unit cell: a section of the tiling, which generates the whole tiling using only translations. Therefore, the volume of the conventional unit cell (Figure 3.1) is always an integer multiple of the primitive cell

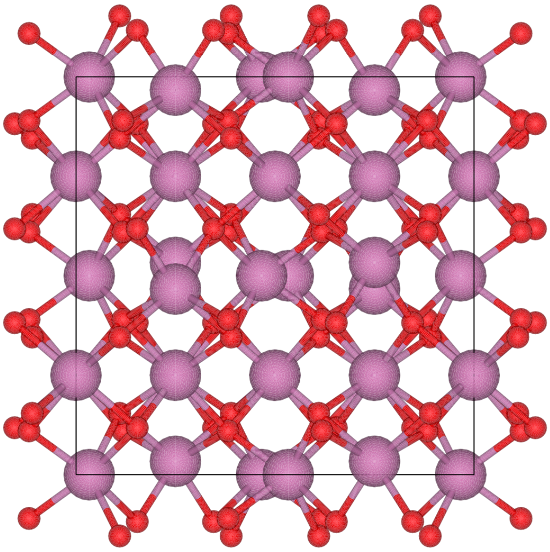

Figure 3.1: Cubic bixbyite structure of the indium oxide conventional unit cell[82].

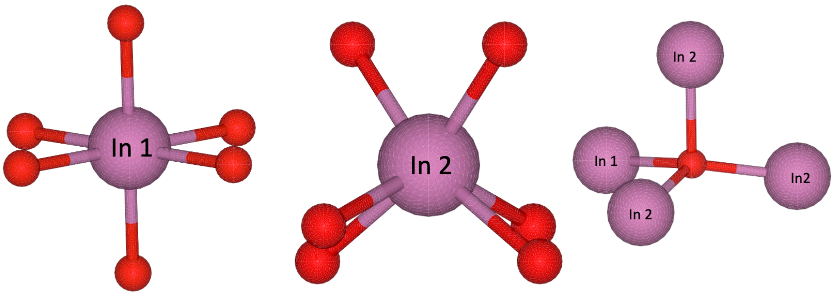

Figure 3.2: Local lattice structures of the In-8*b* (In 1), In-24*d* (In 2) and O-48*e* sites[82].

volume. If a structure is not described by a unit cell smaller than the conventional unit cell, its primitive unit cell is already the conventional unit cell.

In the case of IO, it is possible to describe the full crystal structure by a smaller, primitive unit cell consisting of 40 atoms[83]. The advantage of such unit cell is that it requires much less computing power for DFT calculations, although it is not been investigated if results are as reliable as compared to using the conventional unit cell of 80 atoms. A disadvantage is the limitation for doping. ITO for example, is typically doped to 8% Sn atoms, meaning a substitution of three indium atoms in the conventional unit cell. As the size of the primitive unit cell is half of the conventional unit cell, one and a half indium atom should be replaced. However, it is not possible to do half substitutions for the structure input in DFT softwares.

3.2. Simulation Procedure

In this section the procedure for simulations will be discussed. Simulations in *AMS* are carried out to obtain the real and imaginary dielectric function. *VASP* simulations were performed to obtained the relaxed structure, density of states and band structure. For each simulation step an overview is presented containing the input, calculation principles and the output.

3.2.1. *AMS* Benchmarking

The first software used for simulations was the *Amsterdam Modelling Suite*. A short introduction to the software was given in Section 2.3. Initial simulations using the software were often not successful in the early stages of this thesis due to a lack of computing power. Therefore it was decided to benchmark the software and decide which settings of the simulation could reduce computing time while still giving reasonable results.

For each simulation carried out in *AMS*, the unit cell of the structure is part of the input. These can be built by the user in the input interface or imported from an external software like VESTA[84]. Alternatively, the *AMS* software package comes with an extensive database of pre-optimized structures, including the unit cells of many crystals. The conventional unit cell of IO is among the structures available in this database and will be used as input for the simulations in this section. An advantage for the pre-optimized structures is that DFT geometry optimization has already been done, which normally is a very time consuming step.

Choosing the right basis sets & XC functional

As described in chapter 2, DFT software is not a magical ”black box” which solves the system using only the input. Instead, some key settings need specification. In *AMS*, the most important settings are the basis set and XC functional, which have already been introduced in sections 2.4.4 and 2.4.1 respectively.
As most literature on DFT for IO-like structures use pseudopotential softwares like *VASP* and *Quantum ESPRESSO*, which do not use a basis set, there is not much knowledge on which basis set to use. However, a larger basis set generally leads to higher accuracy, but also increases computational time significantly. Therefore, benchmarking simulations were carried out on IO using basis sets ranging from *SZ* to QZ_4P.
Besides varying the basis set, different XC functionals were also tested. The most popular basis sets from literature are *LDA*, *PBE* and *HSE06*[15, 34–36, 60, 61, 65].

Table 3.1: Benchmark simulation results for IO using different XC functionals and basis sets. The structure input is the conventional 80 atom unit cell provided by the *AMS* database. The calculated properties are the band gap (BG) and the final bond energy (FBE). The computational time is also given.

		Basis Set					
XC-f	**Property**	*SZ*	*DZ*	*DZP*	*TZP*	TZ_2P	QZ_4P
LDA	BG [eV]	1.16	1.44	1.47	1.49	1.51	1.49
	FBE [eV]	-450	-480	-489	-495	-505	-515
	Time [s]	143	235	437	537	974	2,183
PBE	BG [eV]	1.18	1.51	1.54	1.58	1.60	1.58
	FBE [eV]	-383	-416	-424	-432	-441	-448
	Time [s]	152	232	437	559	1,039	2,320
HSE06	BG [eV]	2.01	-	-	-	-	-
	FBE [eV]	-150,838	-	-	-	-	-
	Time [s]	58,920	-	-	-	-	-

The results presented in Table 3.1 show a clear trend going from a small basis set (*SZ*) to a large one (QZ_4P). For both the *LDA* and *PBE* XC functionals, a larger basis set yields a higher band gap and smaller bonding energy, thus becoming a more accurate solution according to the variational theorem[42]. Besides, a larger band gap is obtained using larger basis sets, although still heavily underestimating the experimental band gap of 2.9 eV[85, 86]. However, the relative gain in accuracy of the simulation seems to decrease drastically for basis sets larger than *TZP*. Where for *LDA* and *PBE* the computing time increases with 81% and 86% respectively, their FBE dropped with only about 2% for both XC functionals. Besides, similar band gap values were found for using the *TZP* basis set as with the QZ_4P basis set. Therefore, for further simulations the *TZP* basis set was chosen in *AMS*.

A surprising result was obtained for the computing time, as only an increase of roughly 4% was observed by switching from *LDA* to *PBE*. The *PBE* XC functional is widely regarded as a more accurate XC functional as seen in Figure 2.2. Therefore, upgrading from *LDA* to *PBE* comes at a relative low cost. Upgrading to the more precise *HSE06* XC functional comes with high computational power and is therefore not used in further *AMS* simulations.

Primitive vs. conventional unit cell

As simulations in *AMS* using the conventional 80 atom unit cell for IO take a very long time, it was investigated if the conventional unit cell could be replaced by the smaller primitive unit cell. This primitive unit cell consists of 40 atoms, with the structure shown in Figure 3.3. Similar to the 80 atom unit cell, simulations were carried out using different basis sets and XC functionals.

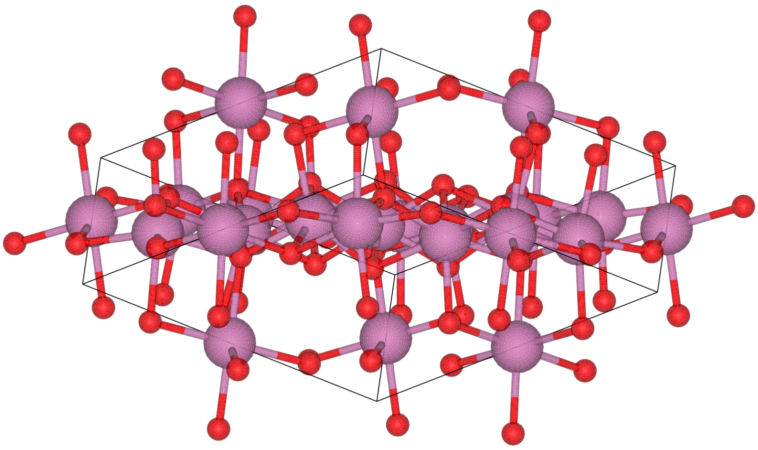

Figure 3.3: Representation of the primitive unit cell of IO[82].

Table 3.2: Benchmark simulation results for IO using different XC functionals and basis sets. The structure input is the primitive 40 atom unit cell provided by the *AMS* database. The calculated properties are the band gap (BG) and the final bond energy (FBE). The computational time is also given.

		Basis	**Set**				
XC-f	**Property**	*SZ*	*DZ*	*DZP*	*TZP*	TZ_2P	QZ_4P
LDA	BG [eV]	2.54	2.79	2.81	2.82	2.85	2.91
	FBE [eV]	-224	-241	-245	-249	-253	-258
	Time [s]	91	126	201	221	335	633
PBE	BG [eV]	2.57	2.86	2.88	2.91	2.94	2.92
	FBE [eV]	-190	-207	-212	-216	-220	-224
	Time [s]	97	126	203	235	365	661
HSE06	BG [eV]	3.62	-	-	-	-	-
	FBE [eV]	-75,421	-	-	-	-	-
	Time [s]	28,932	-	-	-	-	-

From Table 3.2 it is clear that using the smaller, primitive unit cell reduces computing time significantly. For the *PBE* - *TZP* simulation for example, this reduction is 58%. This reduction becomes even larger for when larger basis sets are used.
The final bond energy is quite consistent between the primitive and conventional unit cells. For each simulation using the primitive unit cell, the *FBE* is about half with respect to the simulation using the conventional unit cell. This is expected, as the primitive unit cell is also half the size of the conventional unit cell.

For each combination with basis set and XC functional, the results for the conventional and primitive unit cells differ severely. The calculated band gap is for the primitive unit cell much higher than for the conventional unit cell. Surprisingly, it comes closer to the experimental band gap of 2.9 eV[85, 86]. However, keeping the structural band gap underestimation for the *LDA* and *PBE* XC functionals in mind, these results are not consistent with literature. Another downside to using the primitive unit cell for doping simulations is that limited dopant ratios are possible. The doping resolution would become twice as small when using the primitive cell. Due to the mentioned inconsistency and the low doping resolution, the primitive unit cell will not be used as input for further simulations.

3.2.2. *VASP* Procedure

Geometry optimization simulations in *AMS* had trouble converging due to a lack of computing power. It was decided to use the *Vienna ab initio Simulation Package* for further simulations. *VASP* uses a different simulation approach as described in Section 2.3. The use of pseudopotentials for the non-valence electrons of the structure lowers the degrees of freedom of the system, thus lowering the computing power needed for convergence. In this section, the procedure for *VASP* calculations are presented to obtain the density of states and band structure, as well as the macroscopic properties that can be derived from these.

In the following subsections, a step-by-step guide is presented to describe the simulations to be carried out to obtain the desired results. All *VASP* simulations require at least the following four input files:

1. The POSCAR file contains the structure of the system in terms of lattice geometry and the atom positions in the unit cell.

2. The POTCAR file consists of the pseudopotentials of each atomic species used in the POSCAR file, which describe the core electrons of the system. POTCAR files for all atomic species are provided with the *VASP* license.

3. The INCAR file determines what the simulation should do, and how it should be done[46]. Information provided in this file include the chosen XC potential (Section 2.4.1), cut-off energy (Section 2.4.3) and type of calculation. For each simulation in *VASP*, the *PBE* XC functional[58] is used, unless stated otherwise.

4. The KPOINTS file contains information on the k-points mesh: a finite number of points in the Brillouin Zone (BZ). For all simulations in *VASP*, the Brillouin Zone is sampled using the Monkhorst-Pack k-point mesh of 3 x 3 x 1[87], as this has previously been used in DFT calculations on indiumoxide[35]. The BZ is defined as a unique primitive cell in reciprocal space. It has several point of high symmetry that are of special interest, which are called critical points[88]. These critical points will later be used in the band structure determination.

Step 1: Structure Relaxation

The first step in the simulation procedure is the structure relaxation. The goal is to optimize the structure in such way that the final bond energy is minimized. The POSCAR file for this step contains the structural coordinates and lattice parameters of the conventional unit cell of indiumoxide as shown in Figure 3.1. The POTCAR file is made up from the standard pseudopotentials for Indium and Oxygen. The INCAR file tells the system it should carry out an ionic relaxation calculation with a convergence criterion of 0.01 eV/Å.
Now, the system will be solved iteratively until the specified convergence criterions are met, as described in Section 2.2. The output of interest is the CONTCAR file, which is an adjusted POSCAR file with the optimized lattice parameter and atomic coordinates. This CONTCAR file will then be used as the POSCAR input for further simulation steps.

Step 2: SCF

The second step in the simulation procedure is the self-consistency field calculation. The POSCAR input file is the CONTCAR result of the calculation from step 1, while the POTCAR and KPOINTS input files are equal to step 1. The INCAR file specifies that no ionic movement is allowed and that it only re-optimizes the system for the electronic degrees of freedom, with an energy convergence criterion of 1E-6 eV.
Again, the system will be solved iteratively according to the self-consistency loop (Figure 2.1). The output file of interest is the CHGCAR file, which contains information on the optimized total charge density of the system. This file is then used as the fifth input file in the density of states and band structure simulation steps.

Step 3: Density of States

After obtaining the optimized structure in step 1 and the optimized charge density in step 2, a density of states calculation is carried out in the third step. The POSCAR input is the results from step 1, the CHGCAR input the result from step 2 and the POTCAR and KPOINTS inputs are similar to the previous steps. In the INCAR file it is specified that a density of states calculation should be carried out, including the partial density of states for each orbital type (s, p and d) for each individual atom.

The output of this simulation is the DOSCAR file, which contains the DOS and pDOS of the system for a determined number of energies. This number can be increased to reach higher accuracy in the graph.

Step 4: Band Structure

For band structure determination a highly dense k-point grid is necessary, as only then the band structure will be completely defined. For this, the *SeeK-path* tool is used, which computes all high-symmetry k-points coordinates using a crystal structure as input[89]. The tool returns the k-point path, which is used as the KPOINTS input file for the band structure simulation. Besides, the first BZ and its critical points are determined, which is shown in Figure 3.4.The POSCAR, POTCAR and CHGCAR input files are equal to those of the density of states calculation. The INCAR file specifies that no structural and charge optimization should be carried out.

The output is the band structure of the system, from which the valence band maximum (VBM) and conduction band minimum (CBM) can be determined. These can in turn be used to obtain the effective electron- and hole mass, as described in Section 2.5.3.

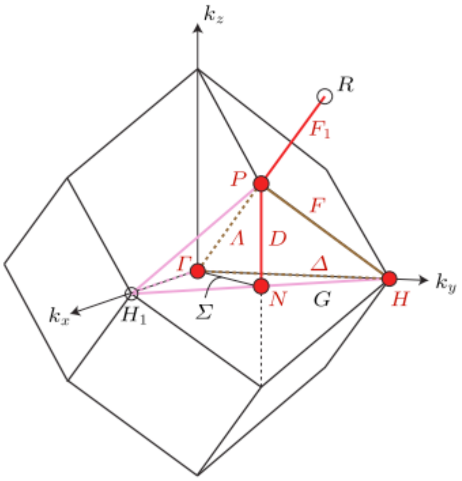

Figure 3.4: Representation of the first Brillouin Zone of IO[90].

Step 5: Hybrid XC functional calculation

To obtain a more reasonable prediction of the band gap, a hybrid XC functional should be used. It has been reported that the *HSE06* XC functional (see Section 2.4.1) provides reasonable prediction of the band gap compared to experiment, but is also very computationally intensive[15, 36, 60, 61, 65].

Step 6: Complex Refractive Index

The dielectric function was obtained by two different methods, using both the *AMS* and *VASP* softwares. For *AMS*, the optimized structure from the *VASP* simulation in step 1 is used as input. Then, the dielectric function is determined in the range from 1-4 eV with 0.1 eV step size. From the dielectric function, the complex refractive index is calculated through the formulas presented in Section 2.5.2.

Step 7: Work Function

The work function of a TCO can be obtained by a slight adjustment in simulation settings from step 3. An additional line should be inserted in the INCAR file (*LVTOT = .TRUE*). Besides, a vacuum layer in the z-direction in the POSCAR of 10 Å is added. The output file (LOCPOT) contains the local potential distribution, with respect to the Fermi energy, in the unit cell and the vacuum slab. The work function can be extracted by taking the potential at the center of the vacuum.

3.3. Validation

In this section, the steps as described in section 3.2.2 are followed to carry out simulations on the conventional IO unit cell. The first step is the geometry optimization. The input structure of IO has lattice parameters *a*=*b*=*c* = 10.29956 Å and a unit cell volume of 1092.59 Å^3. After geometry optimization the lattice parameters are 10.2643 Å, which is in good agreement with the reported experimental value of 10.12 Å[80]. The optimized unit cell volume is 1081.40 Å^3. The geometry optimization has resulted in a unit cell volume reduction of 1.02%. For this structure, such small optimization is expected, as the structure input is already pre-optimized[82].

3.3.1. Density of States

The (partial) DOS for IO was calculated using both the PBE and HSE06 XC functionals. Figure 3.5 shows the total DOS for both XC functionals. Notice that the resolution, the amount of points on the x-axis, is much lower for the HSE06 XC functional, as this method requires a much higher computational load.

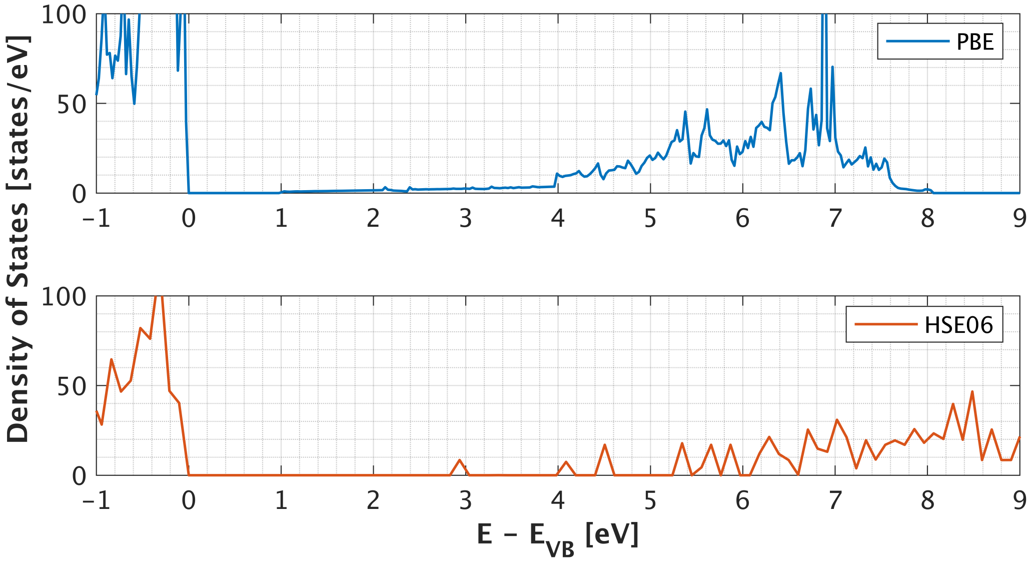

Figure 3.5: IO density of states graph, using both the PBE and HSE06 XC functionals.

The band gap of a material is defined as an energy range where no electronic states can exist. Thus, one can obtain the band gap of IO by taking the energy gap on the x-axis of the DOS graph. From Figure 3.5 we obtain $E_{g,IO}^{PBE} = 1.0254eV$ and $E_{g,IO}^{HSE06} = 2.933eV$. As expected, $E_{g,IO}^{HSE06}$ is consistent with the reported experimental value of 2.9 eV, which was obtained by high-resolution x-ray photoemission spectroscopy[85, 86]. Furthermore, it can be seen that $E_{g,IO}^{PBE}$ severely underestimates the bandgap with respect to the reported experimental value of 2.9 eV. However, this is also expected, as the *PBE* XC functional systematically underestimates the band gap[62]. Keeping this underestimation in mind, results using the *PBE* XC functional can still be useful for showing trends of material properties.

Using the *PBE* XC functional, the partial density of states is also obtained and shown in Figure 3.6. pDOS simulations using the *HSE06* functional are not carried out, as the computational load for this would be too high.

Figure 3.6 shows the pDOS of IO. The third graph shows the contributions of states from the 32 In atoms in the unit cell. The fourth graph shows the contributions of states from the 48 O atoms. Each atom has s-, p-, d- and f-orbitals contributing to the total states. The contribution of f-orbitals is negligible and is thus left out. For simplicity, no distinction within the different s-, p- or d-orbitals is made. Instead, they are bundled together to their corresponding letter.
Again, band gap underestimation is clearly visible in these graphs. Furthermore, it can be seen that

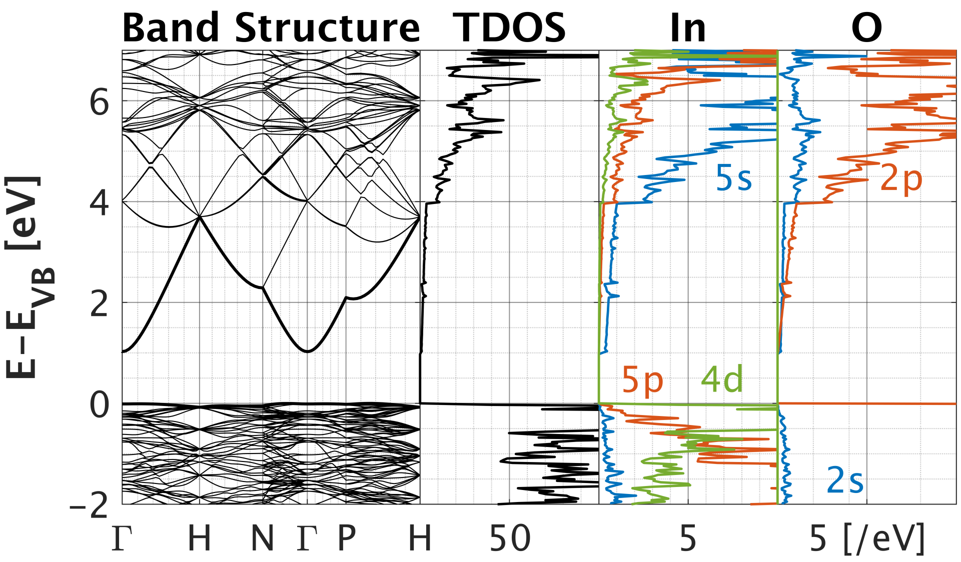

Figure 3.6: Band Structure, DOS and pDOS of IO, simulated with the *PBE* XC functional

the VBM is made up of In-4d and O-2p orbitals. The CBM is made up of hybridization between the In-5s and O-2p orbitals, which is expected from experimental results[91].

3.3.2. Band Structure

The band structure of IO can be obtained by following calculation step 4, as described in Section 3.2.2. Each band is plotted for its energy along the wave vectors, as shown in the left plot of Figure 3.6. The critical points are obtained from the *SeeK-path* tool, a k-path finder and visualizer[89].
In the band structure graph of Figure 3.6 the y-axis represents the relative energy of the band, *i.e.* the band energy corrected with the Fermi energy. The wave vector is represented on the x-axis. The highlighted vectors are given by the letters Γ, H, N and P, which indicate areas in the reciprocal Brillouin zone of the k-space.

Similar to the DOS graphs in Figure 3.6, the band gap can be determined by calculating the energy gap. For the band structure, this is determined by the energy difference between the minimum of the CBM and the VBM, giving $E_{g,IO}^{PBE} = 1.0254eV$. Like the PBE DOS graph, this is again a clear underestimation of the band gap compared to $E_{g,IO}^{HSE06}$. However, this is expected, as for the band structure simulation the *PBE* XC functional was used, which systematically underestimates the band gap of periodic structures[62]. Using the *HSE06* XC functional for band structure simulations is not feasible, as the combination of a hybrid XC functional with a highly dense k-point grid would require enormous computational load. Although the band gap is severely underestimated in the band structure representation, the curvature of the band structure is referable .
Through the band structure one can determine the effective electron mass, using the equations as described in Section 2.5.3 at the edge of the CBM. For IO, this is done for the valley of wave vectors N-Γ-P as shown in Figure 3.6. This results in an effective electron mass of 0.3284m_e^0, which is in good correspondence with the reported experimental value from Hall-effect measurements[92, 93].

3.3.3. Work Function

The work function of IO is obtained by following step 7 of the *VASP* simulation procedure. The local potential is plotted in the z-direction of the unit cell with a 10Å vacuum slab on top, thus corresponding to a (001) surface[94].

From Figure 3.7 the work function can be obtained by taking the energy level of the plateau in the vacuum. This corresponds to $WF_{IO} = 4.2eV$, which is in the acceptable range of the reported experimental value[95, 96].

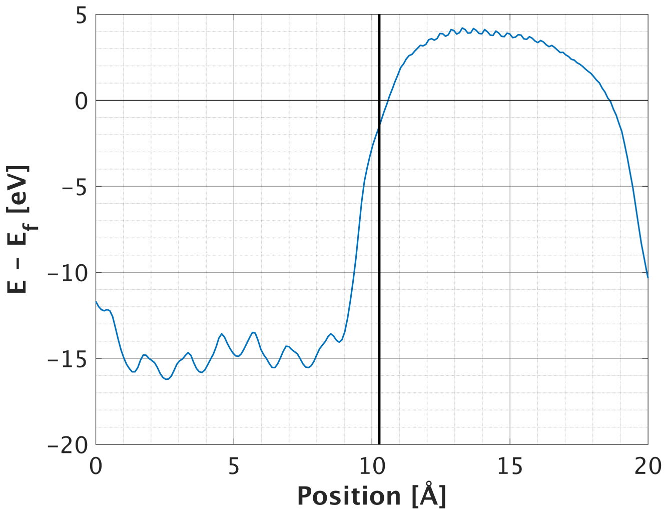

Figure 3.7: Local potential of IO in the z-direction. The vertical line at 10.2643 Å marks the transition point of the IO unit cell to the vacuum slab.

3.3.4. Complex Refractive Index

Experimental results of the complex refractive index was obtained for hydrogenated IO (IO:H) through ellipsometry. These results were tentatively compared to simulated IO *n*,*k*-values from DFT. Figure 3.8 shows the *n* and *k* values of the complex refractive index for IO.

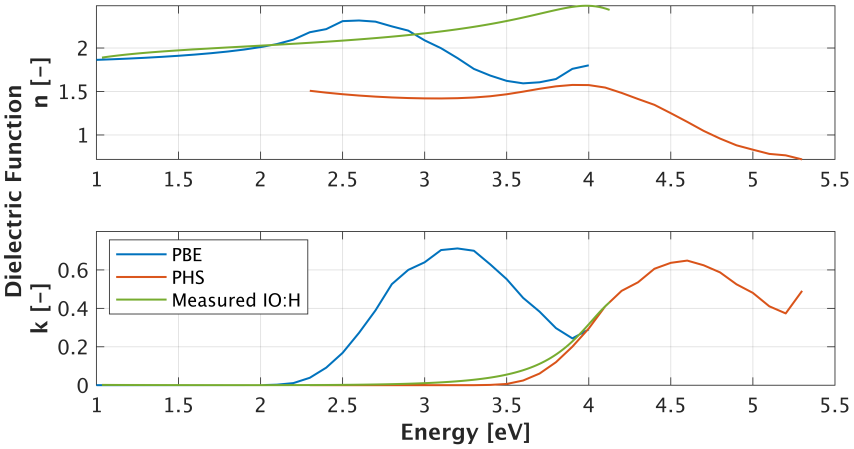

Figure 3.8: Simulated and measured *n* and *k* values of the complex refractive index of IO.

As seen from the measured *k*-value, optical starts slightly below 3 eV and becomes more severe around 3.75 eV, as the curvature increases. This is consistent with reported values from measurement[86, 97, 98]. The PBE-simulated curves clearly show the band gap underestimation of these types of simulations. However, more reasonable complex refractive index predictions can be obtained using the PHS method, as described in Section 2.5.2.

3.4. Conclusions

The goal of this chapter was to compare different methods to obtain the opto-electrical parameters of IO-based TCOs. It became clear that for IO, the structure input plays an important role to get reliable results. Unfortunately, there clearly is a big difference in simulation results when using the conventional IO unit cell compared to the smaller primitive unit cell. Although it was reported that using the primitive unit cell gives reasonable results, we were not able to replicate them. Further investigation in the correct primitive unit cell architecture and simulation settings is necessary to make this work. All further simulations in this thesis are based on the 80 atom conventional IO unit cell.

Next, the basis set influence in the *AMS* software was investigated. It can be concluded that a larger basis basis set yields more reasonable results, as the final bond energy decreases with an increased basis set, thus approaching the ground state energy more closely according to the variational theorem[42]. However, it was found that good accuracy could already be reached with the *TZP* basis set, while requiring much less computational load compared to the larger TZ_2P and QZ_4P basis sets. Therefore, the *TZP* basis set is used in further simulations in *AMS*.

The influence of XC functional has become clear through DOS simulations in *VASP* and band gap calculations in *AMS*. As expected, the band gap is clearly underestimated with the *LDA* and *GGA*-type XC functionals. However, keeping in mind this underestimation, DOS and band structure simulations using the *GGA-PBE* XC functional still give reliable results. Referable band gap prediction could be achieved with the hybrid *HSE06* XC functional, but these simulations require enormous computing power, as expected from the hierarchy ladder of XC functionals shown in Figure 2.2.
Comparable complex refractive index prediction was achieved using the *AMS* software with *PBE* XC functional and the *TZP* basis set. Initial calculations reported, as expected, underestimation of the band gap and therefore a translated complex refractive index. However, translation could be accounted for using the PHS method.
Now that the calculation procedure is set, the next chapters will focus on various IO-based TCOs.

4

Case Study: IO with different dopants

To answer the third research question, a case study on various IO-doped TCOs is carried out. To include a wide variety of possibilities, dopants from post-transition metals (Sn), anionic doping (F) and transition metals (Mo and W) are included with varied doping ratios.
First, an overview of the simulated compounds is presented, where the band structure and DOS graphs are given for the commonly used doping ratios, followed by work function and dielectric function determination. By investigating these parameters, the third research question will be answered: *Can DFT be used to qualitatively or quantitatively examine the opto-electrical parameters of different IO-doped TCOs?*

4.1. Doping Site Preference

In Chapter 3.1 it was shown that within the IO unit cell, two distinct In sites exist: the Wyckoff 8*b* and 24*d* sites. From Figure 3.2 it was shown that the two sites are very similar in geometry, where the 24*d* site is slightly less symmetric than the perfectly symmetric 8*b* site. The (post-)transition metals replace an In site when doped on the IO host. It is well known from experiment that the post-transition metal Sn dopes on the 8*b* site, where the transition metal Mo dopes on the 24*d* site[15].
Steps 1 and 2 of the *VASP* simulation procedures, as described in Section 3.2.2, yield the relaxed structure and its charge density field, from which the ground-state energy (E_0) is calculated by the software. Suggested by [15], we chose different preferable In sites for doping introductions. Comparing E_0 of both site introductions might give an indication as to which site is most preferable. This is done for the doped compounds ITO, IMO and IWO, of which the results are shown in Table 4.1.

Table 4.1: Calculated ground state energy (E_0) for ITO, IMO and IWO, with the Sn, Mo and W dopants substituting an In-8*b* and In-24*d* site respectively. For each compound, one In atom was replaced by a doping atom, corresponding to a x/In doping ratio of 3.1%.

Compound	**doping**	**E_0 [eV]**	**Unit cell Volume [Å^3]**
ITO	Sn^{8b}	-451.07	1083.74
	Sn^{24d}	-451.01	1083.78
IMO	Mo^{8b}	-456.96	1083.55
	Mo^{24d}	-457.24	1084.63
IWO	W^{8b}	-459.75	1086.96
	W^{24d}	-460.05	1087.89

In Table 4.1 it can be seen that a lower ground state energy is calculated when Sn dopes on a 8*b* site compared to when a 24*d* site is doped. For Mo is is the other way around, where a lower ground state energy is calculated when Mo dopes on the 24*d* site. Thus, an indication of the preferable doping sites for Sn and Mo on IO is made by these DFT calculations.
The preferable doping site for IWO is, like for IMO, expected to be on the 24*d* site, as W is a transition metal in the same group as Mo. This is also indicated by the E_0 calculations shown in 4.1.

Table 4.1 also shows the unit cell volume of the relaxed structures. Non-doped IO has a unit cell volume of 1081.40 Å^3. It can be seen that the cell volume is expanded more when the 24*d* site is doped. This can be disadvantageous for the IMO and IWO compounds when deposited on a solar cell, as it might cause distortion in the lattice alignment between the TCO unit cell and the absorber layer unit cell.

4.2. Band Structure and DOS

Steps 3 and 4 of the *VASP* simulation procedure, as described in Section 3.2.2, yield the DOS and band structure respectively. To compare the effect of different types of dopants, the band structure and DOS have been simulated for ITO, IMO, IWO and IFO for their commonly used doping ratios[15, 37, 38]. The calculated band structure and DOS of IO is already presented in Chapter 3 and will be used as reference. As by doping, the unit cell gets slightly distorted, the critical points given on the x-axis of the band structure plot differ.

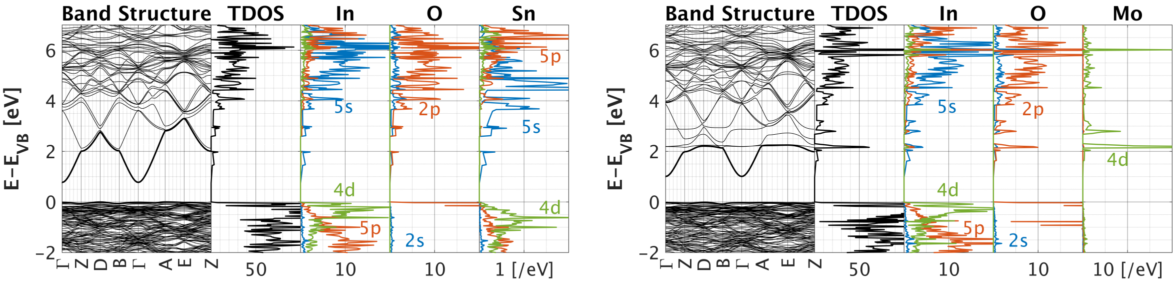

(a) ITO$^{8b}_{9.4\%}$ (b) IMO$^{24d}_{3.1\%}$

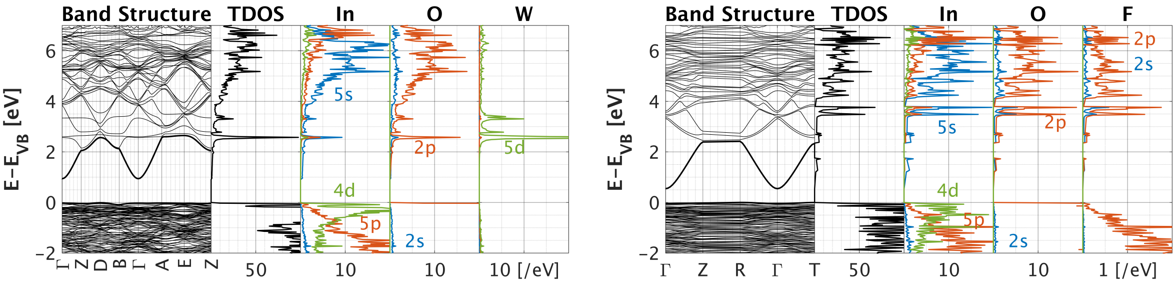

(c) IWO$^{24d}_{3.1\%}$ (d) IFO$^{48e}_{10.4\%}$

Figure 4.1: Band structure, DOS and pDOS graphs for the TCOs ITO, IMO, IWO and IFO in their commonly used doping ratios.

DOS Analysis

It is known that the primary component of the VBM is the O-2p states[91]. From the pDOS graphs in Figure 4.1 it can be seen that the In-4d also contributes to the VBM. The conduction band consists mostly of In-5s and O-2p states. This hybridization of these states is observed for all TCO compounds. Figure 4.1a suggests that conduction band hybridization with the Sn-5s and valence band hybridization with the Sn-4d states occurs. This is in good agreement with reported results on ITO[15, 91].

Figure 4.1b shows that there is large contribution of Mo-4d states just above the conduction band. Besides, it does not appear to show hybridization of the Mo-5s states with the conduction band or valence band. This effect has been observed before[15].

Figure 4.1c shows that there is large contribution of W-5d states just above the conduction band. Besides, no hybridization with the conduction band and valence band of the host is observed. Therefore, the behaviour of W in IWO is very similar as that of Mo in IMO. As for neither transition metals any hybridization of the s- or p-orbitals with the conduction band or valence band is observed, it is expected that these TCOs have a sharper band structure around the Γ-point and thus a lower effective electron mass. This would mean that transition metal doping might be beneficial for obtaining TCOs with high carrier mobility. This is of critical importance for the PV community, since high mobility means that one can achieve highly conductive transparent electrodes without causing parasitic absorption from TCOs[24].

Figure 4.2d shows significant contribution of the F-2p states above the conduction band and below the valence band. Such significant hybridization of doping to the host material also influences the band structure and relevant fundamental parameters, as m_e^*, which will be discussed in the following section.

Band Structure Analysis

Figure 4.1a shows the simulated results for ITO with a Sn/In doping ratio of 9.4% on the 8*b* site. The band curvature surrounding the Γ-point results in an effective electron mass of $0.2360 m_e^0$. This is within the range of experimental results[99]. A band gap at the Γ-point of 0.77 eV is observed.

Figure 4.1b shows the simulated results for IMO with a Mo/In doping ratio of 3.1% on the preferable 24*d* site. The band curvature surrounding the Γ-point results in an effective electron mass of $0.2268 m_e^0$, which is in excellent agreement with simulation results from literature, where the more precise *HSE06* XC functional was used in the simulation[15]. A band gap at the Γ-point of 1.01 eV is observed. Therefore, it can be noted that the *PBE* XC functional gives good band structure predictions, keeping in mind the band gap underestimation, for IMO as well.
In contrary to the band structure obtained through DFT for IMO in literature[15], IMO does not show bands between the CBM and VBM of the IO host. This could be explained by the fact that the standard Mo pseudopotential was used instead of the Mo_d pseudopotential. The Mo_d pseudopotential treats the electrons in the 4d-shell as valence electrons, therefore adding degrees of freedom to the system. The flat band seen just above the CBM in Figure 4.1b is not observed in any of the other band structures. Therefore it is expected that the contribution of this band comes from the Mo-doping, which has been observed before[100].

Figure 4.1c shows the simulated results for IWO with a W/In doping ratio of 3.1% on the preferable 24*d* site. The band curvature surrounding the Γ-point results in an effective electron mass of $0.2307 m_e^0$, which is lower than the effective mass observed for ITO. This provides supportive information to interpret our previous observations in[38]. A band gap at the Γ-point of 0.94 eV is observed.

Figure 4.2d shows the simulated results for IFO with a F/O doping ratio of 10.4% on the 48*e* site. The band curvature surrounding the Γ-point results in an effective electron mass of $0.3116 m_e^0$. This effective mass is relatively high compared to the other TCOs given above, with a value close to the effective mass of un-doped IO. This is expected from the pDOS graphs, as large hybridization of the F-2p states is observed. From the CBM and VBM at the Γ point, a band gap of 0.55 eV is extracted. These results might provide a perspective to understand the contact resistance study between IFO and doped silicon layers, which is still ongoing.

Interestingly, IFO, which shows notable hybridization between doping states and the host CBM, thus resulting in a large m_e^* and low E_g, exhibits higher electron mobility and comparable E_g as compared to ITO from experimental data[37, 101, 102]. We presume this could be related to two aspects. On the one and, from physical definition, the carrier mobility is calculated by $\mu_e = \frac{e\tau_c}{m_e^*}$, in which τ_c is the carrier relaxation time. Plausibly, the IFO could show a high τ_c in nature due to a possible less unit cell distortion compared to the other TCOs[103]. This could be a results of the ion radius of F^- being close to that of O^{2-}. Besides, F has reported to passivate defects such as oxygen vacancies and grain boundaries[104]. On the other hand, the shape of the conduction band needs to be taken into consideration when we interpret E_g. It is well known that, in degenerated semiconductors, the E_g is influenced by the fundamental E_g and a E_g widening due to the so-called Bustein-Moss shift[23, 25]. However, a so called band gap renormalization is mainly reflected by the non-parabolic shape of the host conduction band, which could be adjusted by electron-exchange interactions, and hybridization of the host conduction states from impurity doping[85, 99]. Therefore, the interpretation of the opto-electrical properties is a complicated topic, which needs to be explored with both improved simulations and elaborate experimental investigations.

The TCOs doped with the transition metals Mo and W show a lower effective electron mass compared to the most used TCO , ITO, doped by the post-transition metal Sn. Therefore, with respect to electron transport, IMO and IWO are presumably superior to ITO. These findings support experimental results[15, 38].

4.3. Hybrid XC functional: DOS

In Section 3.3.1 it was observed that referable band gap predictions could be obtained for IO using the *HSE06* hybrid XC functional. Similar simulations were carried out for ITO, IMO, IWO and IFO in their commonly used doping ratios. Their results are shown in Figure 4.2. Unfortunately, the IMO simulation using the *HSE06* functional would not converge and is therefore not included in the figure.

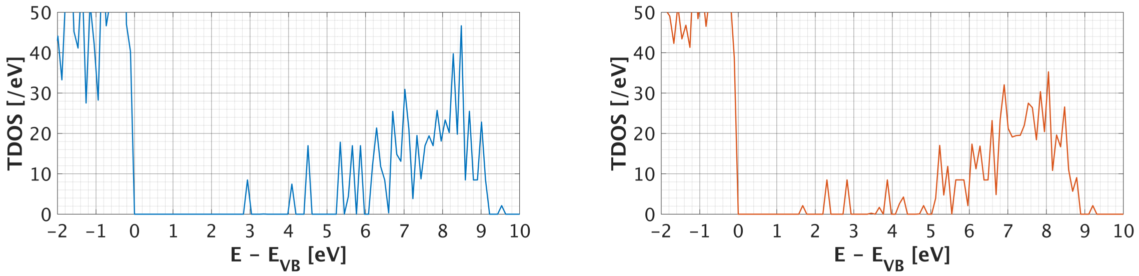

(a) IO

(b) ITO$^{8b}_{9.4\%}$

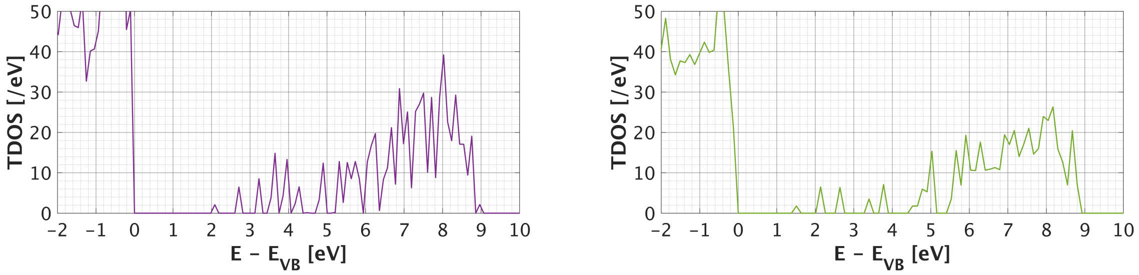

(c) IWO$^{24d}_{3.1\%}$

(d) IFO$^{48e}_{10.4\%}$

Figure 4.2: Density of States for IO, ITO, IWO and IFO, simulated using the hybrid *HSE06* XC functional.

In Section 3.3.1 it was verified that the *HSE06* XC functional can produce reliable predictions of the band gap by reading the DOS of the TCO host IO. For the doped TCOs, the band gaps can be extracted from Figure 4.2. The extracted band gap values are $E_{g,ITO}^{HSE06} = 1.70eV$, $E_{g,IWO}^{HSE06} = 2.18eV$, $E_{g,IFO}^{HSE06} = 1.60eV$ for ITO, IWO and IFO respectively and thus significantly lower than the band gap for IO of 2.9 eV. This is not in line with the trend observed from literature, where it was found that the band gap increases for doped IO. For IWO and IMO, a possible explanation might be the following. From the DOS graphs in Figure 4.2 it can be seen that the peaks corresponding to the CBM are very low and that there is no transition of these peaks into the rest of the states above the CBM. This might suggest that these peaks actually contribute to midgap states caused by the doping, which has been observed before for IMO[15]. This would also suggest that the apparent band gap is actually higher than that of IO, which could be explained by the Moss-Burstein effect. This is caused by the partially occupied states in the conduction band and thus widens the band gap following Pauli's exclusion principle. To investigate if there are indeed midgap states present, band structure simulations using the hybrid *HSE06* XC functional are needed using a highly dense k-point grid. In this thesis, this was done for the *PBE* XC functional as shown in Section 4.2. For the *HSE06* XC functional it is expected that simulations like this might take weeks, even when using a powerful server. Therefore, it was not feasible to do this within the time frame of this thesis.

4.4. Work Function

The work function was determined for the TCOs in their commonly used doping ratios. E_{VB} is determined by the band structure simulation (VASP step 4). From the work function and the valence band energy one can determine the ionization energy (IE), as described in section 2.5.1.

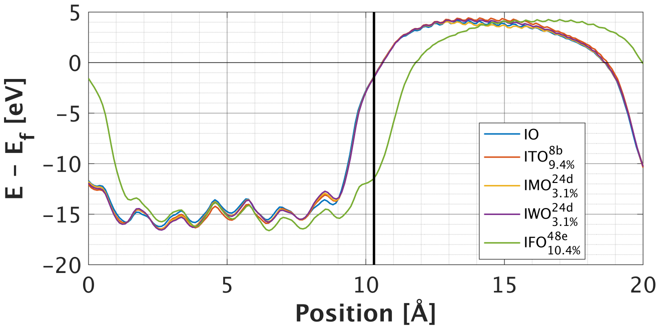

Figure 4.3: Local potential in the z-direction for IO, ITO, IMO, IWO and IFO in their commonly used doping ratios. The vertical line indicates the intersection between the unit cell and the vacuum slab.

From the local potential plot in Figure 4.3, the work function is determined by taking the value of the plateau in the vacuum slab region. The ionization energy (IE) can then be calculated as $IE = E_{VB} - WF$, as both E_{VB} as WF are simulated with respect to the Fermi energy (E_f) in *VASP*. The results are given in Table 4.2.

Table 4.2: Work function, valence band energy and ionization energy and band gap of IO, ITO, IMO, IWO and IFO in their commonly used doping ratios.

Compound	WF [eV]	E_{VB} [eV]	IE [eV]
IO	4.2006	-0.4816	-4.6822
$ITO^{8b}_{9.4\%}$	4.4249	-2.7653	-7.1902
$IMO^{24d}_{3.1\%}$	4.0409	-2.1786	-6.2195
$IWO^{24d}_{3.1\%}$	4.2908	-2.5065	-6.7973
$IFO^{48e}_{10.4\%}$	4.2595	-3.3510	-7.6105

The data shown in Table 4.2 is not realistic, due to uncertainties involved in determining the valence band- and conduction band energies using the *PBE* XC functional. However, the relative energy position change in different types of TCOs may still provide indicative information for analyzing the trend in relevant contact properties, for instance, a TCO/doped Si interface. Furthermore, it is recommended to perform improved simulations with the *HSE06* XC functional, such that one may obtain reliable absolute values for the energy levels in the band structure. This will promote meaningful collaborations to bridge simulation work at different scales, from atomistic modelling to device modelling.

4.5. Complex Refractive Index

Dielectric function simulations were carried out in *AMS*, with *VASP*-optimized unit cell geometries as input. The selected XC functional was *PBE*, with the *TZP* basis set. The orientation of the dielectric function was the x-direction. As it is unclear whether the band gap prediction from the *HSE06* XC functional presented in Section 4.3 is trustworthy, the PHS-method is not applied. The complex refractive index is calculated from the dielectric function through the formulas given in Section 2.5.2.

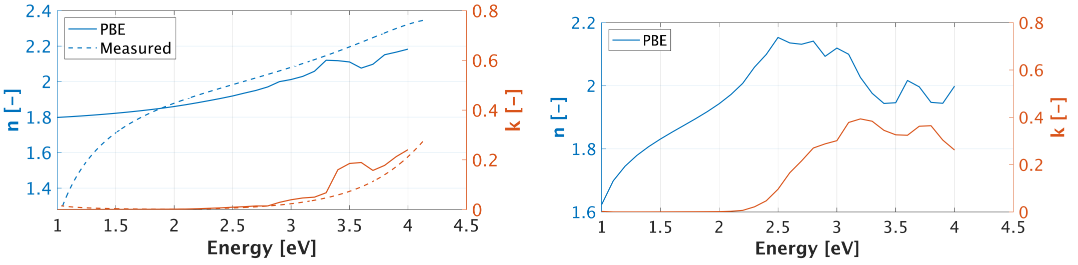

(a) ITO$^{8b}_{9.4\%}$ (b) IMO$^{24d}_{3.1\%}$

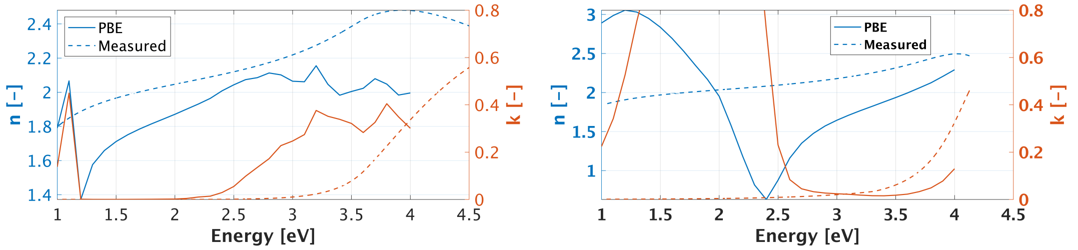

(c) IWO$^{24d}_{3.1\%}$ (d) IFO$^{48e}_{10.4\%}$

Figure 4.4: Complex refractive index of ITO, IMO, IWO and IFO in their commonly used doping ratios.

From the *k*-value of the complex refractive index in Figure 4.4, there is somewhat agreement between simulated and measured results of ITO. This is a surprising result, as from previous simulations in *VASP* there was a clear underestimation of the band gap using the *PBE* functional. It is unclear why this underestimation now is not present.

For IWO there is still an underestimation of the band gap visible. It is shown that the simulated onset of optical absorption starts at a lower energy for IMO and IWO compared to ITO.

For IFO, very high optical absorption in the low energy range is observed. Compared to the measured value, this is clearly not correct. Possibly, the direction in which the dielectric function is obtained is wrong. Further research and improvements need to be done to investigate why this is the case.

In general, the match between measured and simulated results of the complex refractive index is not acceptable, and further improvements need to be done. A possible solution could be to simulate the dielectric function with a much denser k-point grid. In previous work this has proven to work, for much smaller unit cells of GaAs, CdTe and InP, containing less than 10 atoms each[76]. As the unit cells used in this thesis are much larger, it was not feasible to do this within the time frame.

4.6. Conclusions

The goal of this Chapter was to investigate whether it is feasible to develop DFT simulations to obtain the opto-electrical parameters of different IO-based TCOs qualitatively and/or quantitatively. A case study was carried out using different types of doping, being post-transition metal (Sn), transition metal (Mo and W), and anionic (F) doping.

A method was presented to verify the preferable doping site in IO for each doping, by investigating the ground state energy. The preferable 8*b* and 24*d* site for ITO and IMO were verified[15]. Also it was found that the preferable doping site for IWO is the 24*d* site. This was expected, as W is in the same group as Mo.

Band structure and (p)DOS results were obtained and analyzed for ITO, IMO, IWO and IFO in their commonly used doping ratios. From the pDOS graphs it became clear that in ITO there is hybridization of the Sn states with the CBM and VBM. This effect was not observed for transition metal doping with W and Mo. For IFO, hybridization of the F-states was also observed, resulting in a significantly larger effective electron mass. However, experiment has proven that IFO exhibits high electron mobility[37, 101, 102]. Other parameters , such as the carrier relaxation time, play an additional role in the determination of mobility[103]. This makes the interpretation of the electron mobility a difficult topic, which needs to be explored more with improved simulations and experimental investigations.

DOS graphs were also obtained for the *HSE06* XC functional, indicating the band gap underestimation observed for the *PBE* XC functional once more. However, the band gap obtained from the hybrid DOS graphs still underestimates the experimentally obtained band gap. It was speculated that this might be caused by the existance of midgap states. Additional band structure simulation using the *HSE06* XC functional are needed to investigate if this is indeed the case.

A summarizing table with the results from this chapter is presented in Table 4.3.

Table 4.3: Summarizing table of the results obtained in this chapter.

Compound	**WF [eV]**	**Effective Electron Mass [/m_e]**	**IE [eV]**	**E_g^{PBE} [eV]**	**E_g^{HSE06} [eV]**
IO	4.2006	0.3284	-4.6822	1.0254	2.93
$\text{ITO}^{8b}_{9.4\%}$	4.4249	0.2360	-7.1902	0.7733	1.70
$\text{IMO}^{24d}_{3.1\%}$	4.0409	0.2268	-6.2195	1.0079	-
$\text{IWO}^{24d}_{3.1\%}$	4.2908	0.2307	-6.7973	0.9397	2.18
$\text{IFO}^{48e}_{10.4\%}$	4.2595	0.3116	-7.6105	0.5469	1.60

Now that the influence of different dopants is investigated, Chapter 5 will focus on adjusting the doping ratio for the different TCOs.

5

Case Study: TCOs with varied doping ratios

In Chapter 4 we saw the influence of different dopants on the IO host. The goal of this chapter is to use these same dopants in varied doping ratios, to see what the trend is for the band gap and effective electron mass. From there, it will be speculated how the various IO dopants can be manipulated to design a better performing TCO. By investigating these parameters, the fourth and final research question will be answered: *Can DFT be used to qualitatively or quantitatively analyse the effect of doping ratio on IO-doped TCOs?*

5.1. Indium Tin Oxide (ITO)

As mentioned in the introduction, indium tin oxide (ITO) is by far the most used TCO, typically encountered as an oxygen-saturated composition with 74% In, 18% O and 8% Sn by weight. This means three In atoms need to be substituted by tin (Sn) atoms in the 80 atom conventional unit cell. When doped on IO, Sn substitutes an In atom on the In-8*b*. site[15].

Tin is a post-transition metal in group 14 of periodic table of elements, with an electron configuration of [Kr] $4d^{10}5s^25p^2$. Therefore, its outer shell has one extra 5p electron compared to In. Thus, when IO is doped by replacing one In atom with one Sn atom, one extra free electron is donated to the structure.

For Sn/In doping ratios of 3.1% and 9.4%, the DOS was obtained using the *HSE06* XC functional, which is shown in Figure 5.1. A slight decrease of the band gap is observed, similarly to when the *PBE* XC functional was used.

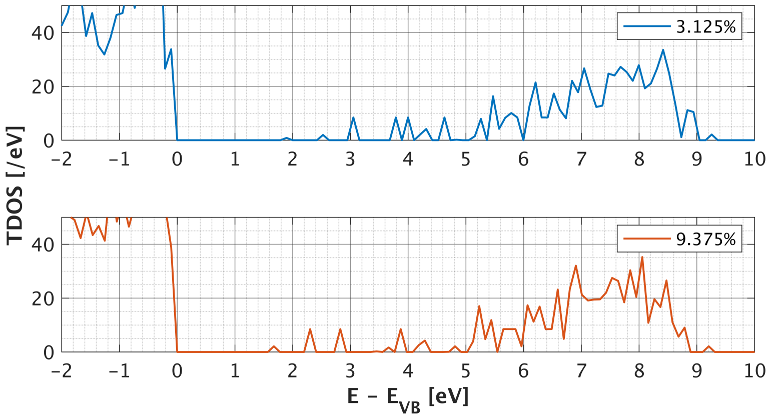

Figure 5.1: Density of States for ITO^{8b} using the *HSE06* XC functional for a Sn/In doping ratio of 3.1% and 9.4%

To visualize the effects of Sn-doping ratio on the (partial) density of states and band structure, simulations were carried out for ITO having one, two or three In atoms replaced on the In-8*b* site, corresponding to Sn/In doping ratios of 3.1%, 6.3% and 9.4% respectively.

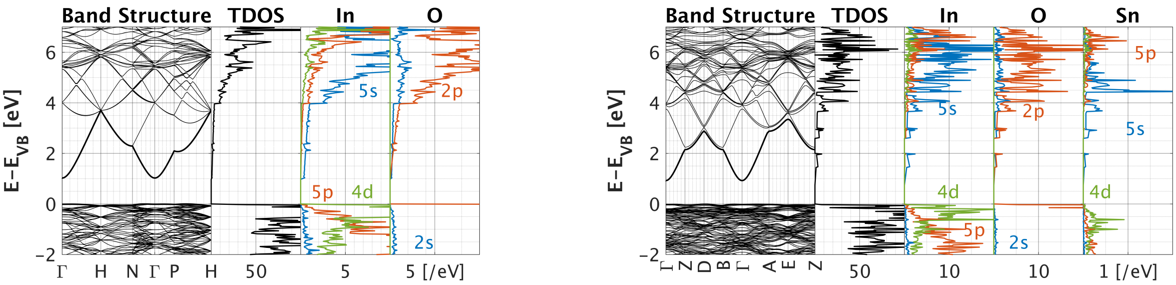

(a) 0%

(b) 3.1%

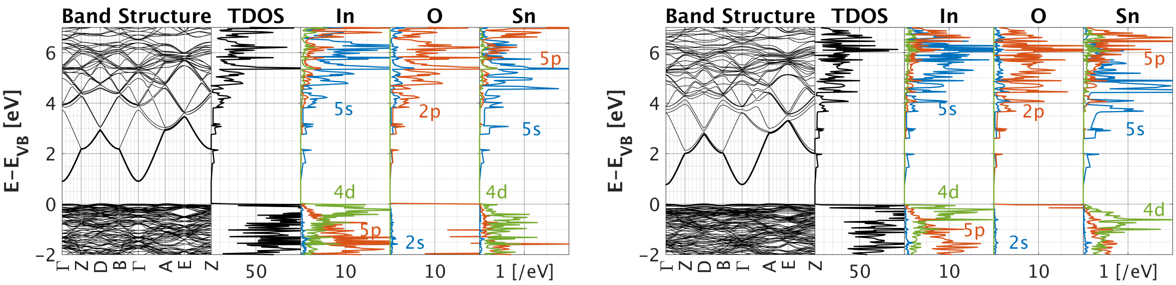

(c) 6.3%

(d) 9.4%

Figure 5.2: Band structure, DOS and pDOS graphs for the TCO ITO with different doping ratios, ranging from 0-9.4%.

The pDOS graphs in Figure 5.2 shows that hybridization takes place between the Sn-doping states and the IO-CBM states. This effect is undesired, as it is expected to widen the CBM and therefore increase the effective electron mass[15]. A higher effective electron mass lowers the electron mobility of the TCO, thus making ITO an inferior TCO when compared to TCOs that do not have hybridization between doping and host states. Besides, it can be seen that this hybridization increases with the doping ratio. Therefore, an increase of the effective electron mass is expected for the higher doping ratios.

Figure 5.2 also shows the band structures of ITO with varied doping ratios. Their shape is very similar, with the CBM at the at the Γ point. However, there is a small difference in the curvature of the CBM and VBM. This leads to the slightly smaller effective electron mass for ITO$^{8b}_{9.4\%}$ of $0.2360m_e^0$, compared to $0.2414m_e^0$ for ITO$^{8b}_{3.1\%}$. Besides a smaller m_e^*, a smaller band gap is also observed. The extracted band gap from the band structure is 0.92 eV for ITO$^{8b}_{3.1\%}$ and 0.77 eV for ITO$^{8b}_{9.4\%}$.

The results for ITO using different doping ratios are summarized in Table 5.1. Note that for the 12.5% doping ratio only the unit cell volume is given.

Table 5.1: Band gap, effective electron mass and unit cell volume for ITO with varied doping ratios.

doping Ratio	**PBE Band Gap [eV]**	**Effective Electron Mass [/m$_e$]**	**Unit cell Volume [Å^3]**
0	1.0254	0.3284	1081.40
3.1	0.9224	0.2414	1083.74
6.3	0.9062	0.2353	1083.78
9.4	0.7733	0.2360	1086.63
12.5	-	-	1088.10

5.2. Indium Tungsten Oxide (IWO)

Like Mo, Tungsten (W) is a transition metal with an electron configuration of [Kr] $4f^{14}5d^{4}6s^{2}$. By tungsten-doping IO to obtain IWO films, In atoms are substituted by W atoms. In experiments done at PVMD, IWO films were deposited with 95 wt% IO and 5 wt% WO_3[38]. For simulations on a 80 atom unit cell, this corresponds to a single In atom being replaced by a W atom. As for IWO we are also interested in the effect of different doping ratios, simulations have also been carried out for 2, 3 and 4 W-dopants per IO unit cell, of which the plots for the band structure and (p)DOS are presented in Figure 5.3.

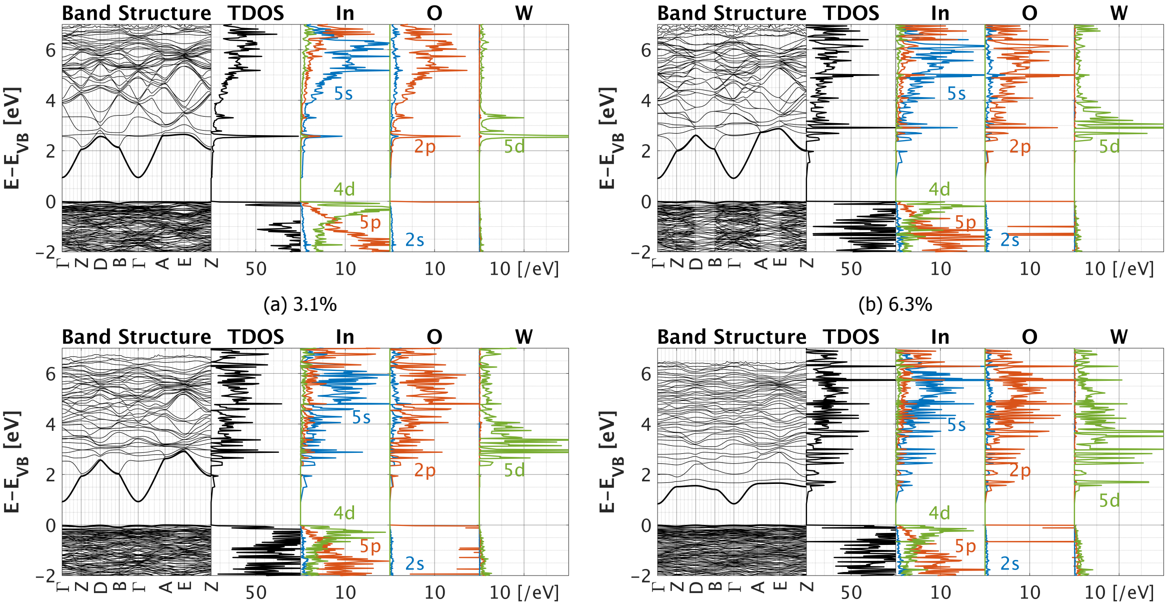

(a) 3.1%

(b) 6.3%

(c) 9.4%

(d) 12.5%

Figure 5.3: Band structure, DOS and pDOS for IWO with varied W/In doping ratios on the 24*d* site.

From the pDOS graphs in Figure 5.3 it can be seen that doping state hybridization with the host CBM becomes significant with an increased doping ratio at 10.4%. This indicates a sharp increase in m_e^*, as obtained from the band structure calculation.
From the curvatures of of the band structures of Figure 5.3 the effective electron mass is obtained. As the curvature up until the 9.3% doping ratio only decreases slightly, its effective electron mass also only increases slightly: from 0.2307-0.2591-0.2719m_e^0. The curvature corresponding to a doping ratio of 12.5% is visibly broader, thus leading to a significant increase in effective electron mass: 0.4639m_e^0. This is in line with the expectation from the pDOS graph of the W-5d states.

The results presented in Figure 5.4 suggest that larger W/In doping ratios are not beneficial for the electrical conductivity of IWO. Due to the unit cell limitations it is unfortunately not possible to simulate lower doping ratios.

For the W/In doping ratios of 3.1 and 6.3%, the DOS was also simulated using the *HSE06* XC functional. A slight decrease in band gap is observed for the higher doping ratio, as was the case with ITO.

Table 5.2 gives an overview of the results obtained on IWO.

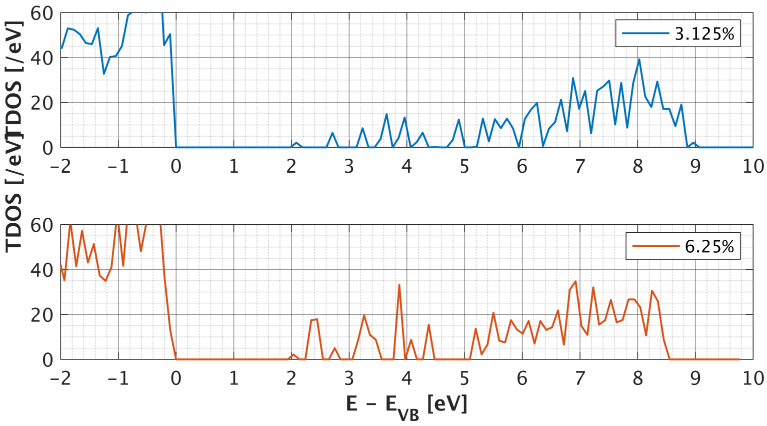

Figure 5.4: Density of States for IWO^{24d} using the *HSE06* XC functional for a W/In doping ratio of 3.1% and 6.3%

Table 5.2: Band gap, effective electron mass and unit cell volume for IWO with varied doping ratios.

doping Ratio [%]	PBE Band Gap [eV]	Effective Electron Mass [/m$_e$]	Unit cell Volume [Å^3]
0	1.0254	0.3284	1081.40
3.1	0.9397	0.2307	1087.89
6.3	0.9085	0.2591	1108.45
9.4	0.9248	0.2719	1110.60
12.5	0.8393	0.4639	1112.48

5.3. Indium Fluorine Oxide (IFO)

Fluorine (F) is a halogen with an electron configuration of [He] 2s^{2}2p^5[105]. It has one electron more than oxygen in its outer shell.

By fluorine-doping IO, O atoms are substituted by F atoms. This is in contrast with tin-, tungsten- and molybdenum-doped IO, where In atoms are substituted. In experiments conducted at PVMD, fluorine doped IO (IFO) had a F/O atomic ratio of 17%[37]. In this thesis, IFO simulations were conducted with doping ratios ranging from 3.1-10.4%. Higher concentrations did not reach convergence and are thus not included.

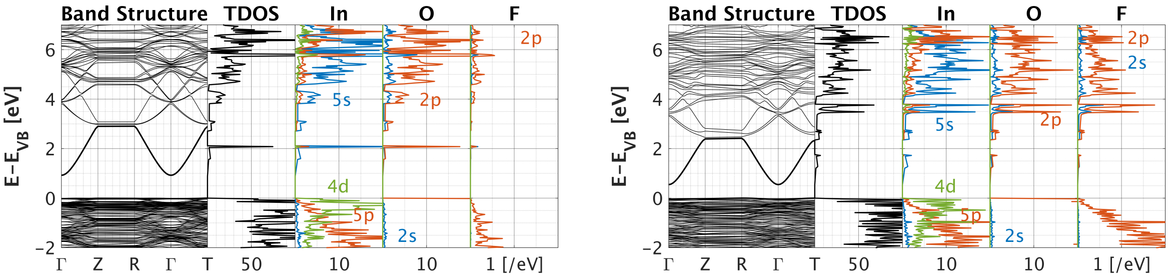

(a) IFO$_{2.1\%}$

(b) IFO$_{10.4\%}$

Figure 5.5: Bandstructure, DOS and pDOS of IFO, with F/O-doping ratios of 3.1% and 10.4%.

From Figure 5.5 an effective electron mass is determined of 0.2875m_e^0 and 0.3116m_e^0. Thus, the effective electron mass appears to increase with a higher doping ratio, as expected and in line with the trend observed from experiment[101].

Experimental results on a pn-junction with IFO/Si pointed out that above a certain F/O doping ratio, the IFO tends to form a diode with p-Si and ohmic contact with n-Si[101]. Therefore, to have good electron conductivity, a very low F/O ratio is required, around 3%. For the 80 atom IO-host unit cell, replacing a single O atom with an F-doping already translates to a F/O ratio of 3.1%. Therefore, it is expected that simulations using this unit cell will already have a large effective electron mass compared to the other TCOs.

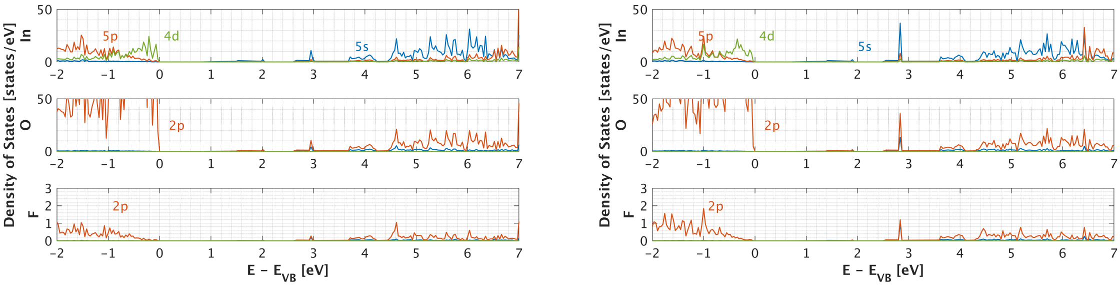

(a) 6.3%

(b) 9.4%

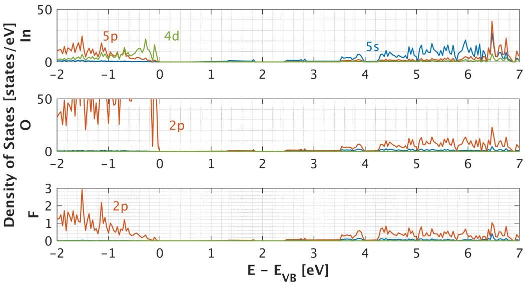

(c) 12.5%

Figure 5.6: pDOS of IFO with varied F/O doping ratios

From the pDOS graphs in Figure 5.6 it can once again be seen that hybridization between the F-doping and IO-host states takes place. This hybridization also appears to increase with higher F/O doping ratios. Thus, it is expected that a higher effective electron mass will be obtained for the higher doping ratios.

For the doping ratios of 2.1 and 10.4% the band structure was also simulated and presented in Figure 5.5.

An overview of the results for IFO is given in Table 5.3. Note that the band gap and effective electron mass for the F/O doping ratios of 4.2%, 6.3% and 8.3% are not given, as the band structure simulations were not converged in time.

Table 5.3: Band gap, effective electron mass and unit cell volume for IFO with varied doping ratios.

doping Ratio [%]	**PBE Band Gap [eV]**	**Effective Electron Mass [/m_e]**	**Unit cell Volume [Å^3]**
0	1.0254	0.3284	1081.40
2.1	0.9226	0.2875	1087.63
4.2	-	-	1092.06
6.3	-	-	1096.72
8.5	-	-	1101.34
10.4	0.5469	0.3116	1106.75

5.4. Overview

To summarize this chapter, Figure 5.7 gives the trend of the optimized unit cell volume, *PBE* simulated band gap and effective electron mass of the different TCOs with varied doping ratios.

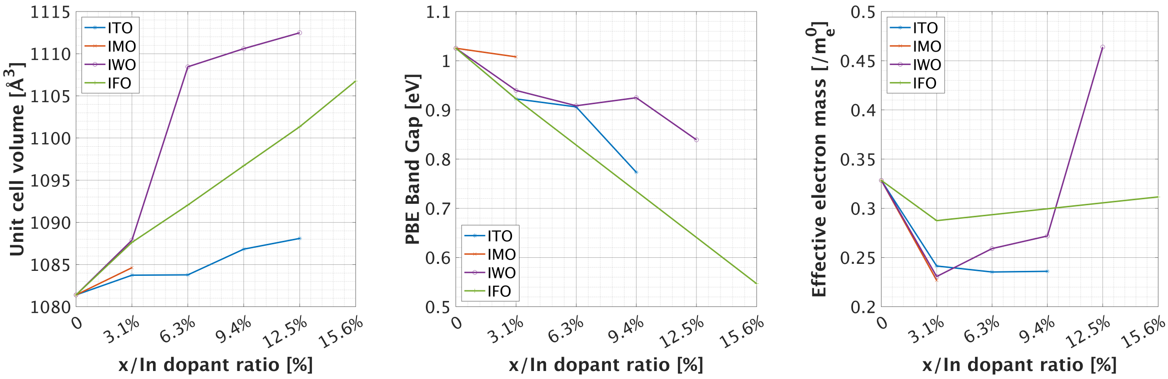

(a) Unit Cell Volume (b) PBE Simulated Band Gap (c) Effective Electron Mass

Figure 5.7: Unit cell volume, band gap and effective electron mass with varied doping ratios

From these Figures the following trends can be observed.
Independently of the doping, the unit cell volume increases with the doping ratio, but especially for IWO. This might be unfavourable for using highly doped IWO as a TCO deposited on a solar cell, since highly doped IWO may bring severe lattice distortion. However, on the other hand, unlike ITO, more effective doping efficiency could be achieved by IWO with low doping ratios. This is caused by the high Lewis acid of the W dopant[106], and the formation of favourable charged complexes[107]. Therefore, IWO may provide a promising option to reach decent opto-electrical properties without introducing high doping ratios in the host material. This might be one reason why IWO has been widely utilized in high efficiency silicon heterojunction solar cell development in recent years.

The band gap decreases with the doping ratio for each doping element. This probably causes more parasitic absorption in the TCO layer, but further investigation on the dielectric function is necessary to examine this.

For low doping ratios, the effective mass decreases. However, for most TCOs, after the first doping step the effective mass increases again. This is a results of the hybridization of the doping states and the CBM of the TCO host. For ITO this is apparently not the case. However, it does not mean that in the ITO case, higher doping ratio is better. Multi-body interactions, either between free carriers and ionized impurities, will limit the optical transitions in the UV region[85]. In addition, severe dopant scattering due to high doping ratios is also detrimental to obtain high carrier mobilities[108].
For IWO and IMO it becomes clear why it is important to keep the doping ratio low. Unfortunately, due to unit cell limitations, lower doping ratios can not be simulated for now.

5.5. Conclusions

The goal of this chapter was to vary the doping ratios of ITO, IWO and IFO and observe the trends. It was observed that hybridization of the doping states and the CBM increases with the doping ratio, thus increasing the effective electron mass obtained from the band structure.

For each doping, the optimized unit cell volume increases with the doping ratio. This is especially the case for IWO. Further research is needed to check what is the appropriate doping ratio range for each type of TCO.

The simulated band gap decreases with the doping ratio. Further research on the simulated dielectric function is needed to examine what the effect is on the parasitic absorption.

6
Conclusions & Recommendations

In the Introduction of this thesis four research questions were presented which needed to be answered to reach the research goals. To conclude, the research questions will be answered here.

1: How does DFT software solve the Schrödinger equation?
In Chapter 2 the fundamental principles of DFT were introduced. DFT software estimates the Schrödinger equation by solving the Kohn-Sham equations iteratively. Part of the Kohn-Sham equations, the exchange-correlation (XC) potential is unsolvable and need to be estimated. Many different approaches of describing the XC potential exist, ranging from highly accurate to very basic. The process converges if the energy difference describing the system is smaller than a pre-set value. We found out that simulation settings play a critical role in getting reliable simulation results. Choosing the right XC functional is especially of importance, as some heavily underestimate the band gap (*PBE*) while others are expected to be very accurate (*HSE06*), although coming at a very high computation time. On top of that, we learned that the *Amsterdam Modelling Suite* works with slater-type orbitals, requiring an additional input parameter: the basis set. The *Vienna ab initio Simulation Package* is based on pseudopotentials, allowing only the valence electrons of an atom to be ”seen” as free electrons, and therefore greatly reducing the computational time.

2: With what simulation settings does DFT software provide results comparable to experiment?
In Chapter 3 the different simulation methods using *VASP* and *AMS* were explored. It was found that usign *AMS*, convergence problems occur when trying to do a geometry optimization for the IO unit cell. We tried solving this issue by using the smaller primitive unit cell. Unfortunately, this was unsuccessful, as the results from the primitive and conventional unit cell proved to be inconsistent. However, the geometry optimization in *VASP* was successful. Therefore, it was decided to only use *AMS* to obtain the dielectric function. VASP would be used to obtain the band structure and density of states.
As expected, the *PBE* XC functional returned heavily underestimated band gap results for IO, with the *HSE06* XC functional providing more reasonable band gap results. Combining the two methods, a satisfying prediction of the complex refractive index could be given, using the PHS-method. Besides, density of states, band structure and work function simulations using the *PBE* XC functional proved to be consistent with literature.

3. Can DFT be used to qualitatively or quantitatively examine the opto-electrical parameters of different IO-doped TCOs?
In Chapter 4, simulations were carried out for doped IO structures, using Sn, Mo, F and W as dopants to make ITO, IMO, IFO and IWO respectively. Hence, post-transition metal-, transition metal- and anionic doping of IO was investigated. The pDOS graphs for ITO showed that hybridization between the Sn-dopant states and the IO-host states takes place. This goes to show that improvements in dopants are still possible. It was indicated that IWO might be a good candidate for an improved TCO[38]. This indication has been supported by the observations in this thesis, as the pDOS graph for IWO showed no detrimental hybridization between the W-dopant states and the IO-host states when doping W on the In-24*d* Wyckoff site. It was also found that the preferable dopant site in IWO is the 24*d* site, similar to IMO[15]. This is in line with expectation, as the dopants Mo and W share the same group in the periodic table of elements.
For IFO, significant hybridization of F-dopant states with the IO host CBM was observed, resulting in a relatively large effective electron mass. However, experiment has proven that IFO exhibits high electrical conductivity[37, 101, 102]. A possible explanation for this discrepancy was given in Chapter 4,

stating that other parameters, like the carrier relaxation time τ_c, play an additional role in carrier mobility determination. It can be concluded that the interpretation of opto-electrical properties is a difficult topic, which needs to be explored more with improved simulations and experimental investigations.

4: Can DFT be used to qualitatively or quantitatively analyse the effect of dopant ratio on IO-doped TCOs?
In Chapter 5 the dopant ratio of the different TCOs was adjusted to see what the effect is on the band gap, effective electron mass and unit cell structure. Simulations showed that the unit cell volume becomes more distorted when the dopant ratio is increased, regardless of dopant type. A reduced trend for the band gap with higher dopant ratios was also observed. This might result in undesirable higher parasitic absorption in the TCO layer, but this needs to be further examined with more precise dielectric function simulations. For IWO and IFO an increasing trend in the effective electron mass is observed with the dopant ratio. Therefore, to be good electrical conductors, it is important to keep the dopant ratio low. For ITO, the effective electron mass does not appear to increase with the dopant ratio, which is probably why ITO is commonly doped in such high concentrations.

This thesis indicates that DFT can be used qualitatively to examine and compare the opto-electrical properties of TCOs, both from different dopants and different dopant ratios. However, it should not be seen as substitution of experiments. DFT is quantitatively still very limited, mostly due to the large underestimation of the band gap, due to the generalised gradient approximation (GGA) XC functional[62, 63]. Still, the trends that can be observed from comparing simulation results from DFT can be useful.

6.1. Recommendations

Preferable Dopant Site after first doping step

In this thesis, the only preferable dopant site that was determined was for the first dopant step, that is, at the lowest possible dopant ratio. Further research could be done on where the dopant atom most likely replaces a second In atom in the unit cell, after one dopant is already present.

Smaller dopant ratio intervals

A downside to DFT softwares is its very high computational load. To reduce computing time, the smallest possible structure is used as input; the unit cell. However, this leads to an enormous step size in dopant ratios. Therefore, it is hard to predict a certain trend when looking at dopant ratios. It would be interesting to get a higher resolution for these trends, although it is expected that this would require enormous computational power.

Different directions unit cell

The work function in this thesis was determined in the z-direction. However, not all sides of the TCO unit cell have the same surface, depending on the dopant position. It would be interesting what the effect is of the different directions. The same is valid for the complex refractive index, which was also determined in one direction only.

Temperature dependence

By default, *VASP* does static calculations, meaning zero K and zero pressure. The formation energy output is therefore also given without considering the entropy value. However, it is possible to smear the electronic results, and by that introducing some temperature dependence. This was not the scope of this thesis, but is definitely worth researching.

Using the In_d pseudopotential

The pseudopotential library that comes with the *VASP* software, containing the POTCAR files, contain multiple options for most elements. In this work, the basic pseudopotential files have been used. It would be interesting to see if calculation accuracy can be improved by using the *d*-state pseudopotentials for the transition metals, as these imply that the *d*-states are treated as valence states. For In, this increases the amount of valence states from 3 to 13, and thus drastically increasing the degrees of freedom for the simulation. As computational time was limited, it was not feasible to do this in this thesis.

p-type TCOs

As of late, p-type TCOs have become a hot topic in exploring novel TCO materials[24]. However, results from this thesis point out that the VBM of IO remains flat, i.e., no significant curvature is observed. This indicates a very high effective hole mass. There have been efforts made on developing p-type IO-based TCOs, which turned out unsuccessful[109]. Therefore, it might be difficult to develop p-type TCOs based on the IO host material. However, various p-type TCOs could be promising for favourable contact engineering, which deserves elaborate investigation in relevant fields.

Introduction of oxygen vacancies and hydrogen doping

The current simulation procedure is based on an ideal crystal unit. In reality, it has been well proven that hydrogen doping and oxygen vacancies play important roles in determining the opto-electrical properties in real TCO films[81, 110].

Amorphous TCOs

Amorphous TCOs, such as IZO[111] and IGZO[112], are also reported to exhibit high carrier mobilities. It can also be an interesting aspect to check how the material phase influences the band structures of TCO materials.

Indium-free TCOs

Lastly, an interesting topic is the search in TCOs that are not based on Indium in the TCO host structure, as Indium is a rare earth metal, and the demand in such materials is rising[24].

Bibliography

[1] E. Becquerel, *Mémoire sur les effets électriques produits sous l'influence des rayons solaires,* Comptes Rendus , 561 (1839).

[2] D. M. Chapin, C. S. Fuller, and G. L. Pearson, *A new silicon p-n junction photocell for converting solar radiation into electrical power [3],* (1954).

[3] F. Ise, *Photovoltaics Report*, Tech. Rep.

[4] M. A. Green, *The path to 25silicon solar cell efficiency: History of silicon cell evolution,* Progress in Photovoltaics: Research and Applications **17**, 183 (2009).

[5] R. S. Ohl, *Light-sensitive electric device*, Tech. Rep. (1946).

[6] R. A. Arndt, J. F. Allison, J. Meulenberg, A., J. G. Haynos, R. A. Arndt, J. F. Allison, J. Meulenberg, A., and J. G. Haynos, *Optical properties of the COMSAT Non-Reflective cell,* pvs , 40 (1975).

[7] K. Yoshikawa, W. Yoshida, T. Irie, H. Kawasaki, K. Konishi, H. Ishibashi, T. Asatani, D. Adachi, M. Kanematsu, H. Uzu, and K. Yamamoto, *Exceeding conversion efficiency of 26% by heterojunction interdigitated back contact solar cell with thin film Si technology,* Solar Energy Materials and Solar Cells **173**, 37 (2017).

[8] L. C. Andreani, A. Bozzola, P. Kowalczewski, M. Liscidini, and L. Redorici, *Silicon solar cells: toward the efficiency limits,* Advances in Physics: X **4**, 1548305 (2019).

[9] D. Adachi, J. L. Hernández, and K. Yamamoto, *Impact of carrier recombination on fill factor for large area heterojunction crystalline silicon solar cell with 25.1% efficiency,* Applied Physics Letters **107**, 23 (2015).

[10] S. DeWolf, A. Descoeudres, Z. C. Holman, and C. Ballif, *High-efficiency silicon heterojunction solar cells: A review,* Green **2**, 7 (2012).

[11] A. Smets, K. Jäger, O. Isabella, R. Van Swaaij, and M. Zeman, *Solar Energy: the Physics and Engineering of Photovoltaic Conversion Technologies and Systems, UIT Cambridge,* **1** (2016).

[12] M. I. Hossain, W. Qarony, M. K. Hossain, M. K. Debnath, M. J. Uddin, and Y. H. Tsang, *Effect of back reflectors on photon absorption in thin-film amorphous silicon solar cells,* Applied Nanoscience (Switzerland) **7**, 489 (2017).

[13] D. S. Hecht, L. Hu, and G. Irvin, *Emerging transparent electrodes based on thin films of carbon nanotubes, graphene, and metallic nanostructures,* (2011).

[14] *Transparent Conductive Films Market Global Forecast to 2026 | MarketsandMarkets,* .

[15] J. E. Swallow, B. A. Williamson, S. Sathasivam, M. Birkett, T. J. Featherstone, P. A. Murgatroyd, H. J. Edwards, Z. W. Lebens-Higgins, D. A. Duncan, M. Farnworth, P. Warren, N. Peng, T. L. Lee, L. F. Piper, A. Regoutz, C. J. Carmalt, I. P. Parkin, V. R. Dhanak, D. O. Scanlon, and T. D. Veal, *Resonant doping for high mobility transparent conductors: The case of Mo-doped In2O3,* Materials Horizons **7**, 236 (2020).

[16] K. Ellmer, *Past achievements and future challenges in the development of optically transparent electrodes,* Nature Photonics **6**, 809 (2012).

[17] A. Kumar and C. Zhou, *The race to replace tin-doped indium oxide: Which material will win?* (2010).

[18] L. Zhang, Y. Zhou, L. Guo, W. Zhao, A. Barnes, H. T. Zhang, C. Eaton, Y. Zheng, M. Brahlek, H. F. Haneef, N. J. Podraza, M. H. Chan, V. Gopalan, K. M. Rabe, and R. Engel-Herbert, *Correlated metals as transparent conductors,* Nature Materials **15**, 204 (2016).

[19] H. C. M. Knoops, B. W. H. van de Loo, S. Smit, M. V. Ponomarev, J.-W. Weber, K. Sharma, W. M. M. Kessels, and M. Creatore, *Optical modeling of plasma-deposited ZnO films: Electron scattering at different length scales,* Journal of Vacuum Science & Technology A: Vacuum, Surfaces, and Films **33**, 021509 (2015).

[20] D. K. Gupta, M. Langelaar, M. Barink, and F. van Keulen, *Optimizing front metallization patterns: Efficiency with aesthetics in free-form solar cells,* Renewable Energy **86**, 1332 (2016).

[21] T. de Boer, M. F. Bekheet, A. Gurlo, R. Riedel, and A. Moewes, *Band gap and electronic structure of cubic, rhombohedral, and orthorhombic* $\mathrm{in}_2\mathrm{o}_3$ *polymorphs: Experiment and theory,* Phys. Rev. B **93**, 155205 (2016).

[22] K. L. Chopra, S. Major, and D. K. Pandya, *Transparent conductors-A status review, Thin Solid Films*, **102**, 1 (1983).

[23] S. C. Dixon, D. O. Scanlon, C. J. Carmalt, and I. P. Parkin, *n-Type doped transparent conducting binary oxides: an overview,* Journal of Materials Chemistry C **4**, 6946 (2016).

[24] M. Morales-Masis, S. De Wolf, R. Woods-Robinson, J. W. Ager, and C. Ballif, *Transparent Electrodes for Efficient Optoelectronics,* Advanced Electronic Materials **3** (2017), 10.1002/aelm.201600529.

[25] T. S. MOSS, G. J. BURRELL, and B. ELLIS, *Chapter 3 - ABSORPTION PROCESSES IN SEMICONDUCTORS,* in *Semiconductor Opto-Electronics*, edited by T. S. MOSS, G. J. BURRELL, and B. ELLIS (Butterworth-Heinemann, 1973) pp. 48–94.

[26] H. Fujiwara and M. Kondo, *Effects of carrier concentration on the dielectric function of ZnO:Ga and In 2O 3:Sn studied by spectroscopic ellipsometry: Analysis of free-carrier and band-edge absorption,* Physical Review B - Condensed Matter and Materials Physics **71**, 075109 (2005).

[27] H. Hosono, *Exploring electro-active functionality of transparent oxide materials, Japanese Journal of Applied Physics*, **52**, 090001 (2013).

[28] S. M. Wie, C. H. Hong, S. K. Oh, W. S. Cheong, Y. J. Yoon, and J. S. Kwak, *Fully crystallized ultrathin ITO films deposited by sputtering with in-situ electron beam irradiation for touch-sensitive screens,* Ceramics International **40**, 11163 (2014).

[29] Vinod, R. Kumar, and S. K. Singh, *Solar photovoltaic modeling and simulation: As a renewable energy solution,* Energy Reports **4**, 701 (2018).

[30] Y.-C. Wu and Y.-R. Jhan, *Introduction of Synopsys Sentaurus TCAD Simulation,* in *3D TCAD Simulation for CMOS Nanoeletronic Devices* (Springer Singapore, 2018) pp. 1–17.

[31] M. Zeman, J. Van Den Heuvel, M. Kroon, J. Willemen, B. Pieters, J. Krč, and S. Solntsev, *Advanced Semiconductor Analysis opto-electronic simulator for amorphous and crystalline semiconductor devices User's Manual*, Tech. Rep.

[32] D. S. Sholl and J. A. Steckel, *Density Functional Theory: A Practical Introduction* (John Wiley & Sons, Inc., Hoboken, NJ, USA, 2009) pp. 1–238.

[33] K. Capelle, *Brazilian Journal of Physics*, Tech. Rep. 4A (2006).

[34] S. H. Brewer and S. Franzen, *Calculation of the electronic and optical properties of indium tin oxide by density functional theory,* Chemical Physics **300**, 285 (2004).

[35] Z. Chen, L. Huang, Q. Zhang, Y. Xi, R. Li, W. Li, G. Xu, and H. Cheng, *Electronic structures and transport properties of n-type-doped indium oxides,* Journal of Physical Chemistry C **119**, 4789 (2015).

[36] A. Walsh, J. L. Da Silva, Y. Yan, M. M. Al-Jassim, and S. H. Wei, *Origin of electronic and optical trends in ternary In 2 O 3 (ZnO) n transparent conducting oxides (n=1,3,5): Hybrid density functional theory calculations,* Physical Review B - Condensed Matter and Materials Physics **79**, 3 (2009).

[37] C. Han, G. Yang, A. Montes, P. Procel, L. Mazzarella, Y. Zhao, S. Eijt, H. Schut, X. Zhang, M. Zeman, and O. Isabella, *Realizing the Potential of RF-Sputtered Hydrogenated Fluorine-Doped Indium Oxide as an Electrode Material for Ultrathin SiO x/Poly-Si Passivating Contacts,* ACS Applied Energy Materials **3**, 8606 (2020).

[38] C. Han, Y. Zhao, L. Mazzarella, R. Santbergen, A. Montes, P. Procel, G. Yang, X. Zhang, M. Zeman, and O. Isabella, *Room-temperature sputtered tungsten-doped indium oxide for improved current in silicon heterojunction solar cells,* Solar Energy Materials and Solar Cells **227**, 111082 (2021).

[39] A. Alcaniz Moya, *Numerical simulation of c-Si solar cells based on transition metal oxide as carrier selective contact,* .

[40] P. Erhart, *A very short introduction to density functional theory (DFT)*, Tech. Rep.

[41] M. Born and R. Oppenheimer, *Zur Quantentheorie der Molekeln,* Annalen der Physik **389**, 457 (1927).

[42] J. Toulouse, *Introduction to density-functional theory Lecture notes for courses given at*, Tech. Rep.

[43] P. Hohenberg and W. Kohn, *Inhomogeneous electron gas,* Phys. Rev. **136**, B864 (1964).

[44] W. Kohn and L. J. Sham, *Self-consistent equations including exchange and correlation effects,* Physical Review **140**, A1133 (1965).

[45] D. G. Truhlar and R. Peverati, *Cite this article: Peverati R, Truhlar DG,* (2014), 10.1098/rsta.2012.0476.

[46] G. Kresse and J. Hafner, *Ab initio molecular dynamics for liquid metals,* Physical Review B **47**, 558 (1993).

[47] G. Kresse and J. Furthmüller, *Efficiency of ab-initio total energy calculations for metals and semiconductors using a plane-wave basis set,* Computational Materials Science **6**, 15 (1996).

[48] G. Kresse and J. Furthmüller, *Efficient iterative schemes for ab initio total-energy calculations using a plane-wave basis set,* Physical Review B - Condensed Matter and Materials Physics **54**, 11169 (1996).

[49] D. Joubert, *From ultrasoft pseudopotentials to the projector augmented-wave method,* Physical Review B - Condensed Matter and Materials Physics **59**, 1758 (1999).

[50] *Amsterdam Modeling Suite Making Computational Chemistry Work For You Software for Chemistry & Materials,* .

[51] P. E. Blöchl, *Projector augmented-wave method,* Physical Review B **50**, 17953 (1994).

[52] C. Rostgaard, *The Projector Augmented-wave Method,* (2010).

[53] A. Dal Corso, *Projector augmented-wave method: Application to relativistic spin-density functional theory,* Physical Review B - Condensed Matter and Materials Physics **82**, 075116 (2010).

[54] J. C. Slater, *Atomic shielding constants,* Physical Review **36**, 57 (1930).

[55] E. Van Lenthe and E. J. Baerends, *Optimized Slater-type basis sets for the elements 1-118,* Journal of Computational Chemistry **24**, 1142 (2003).

[56] Q. Peng, F. Duarte, and R. S. Paton, *Computing organic stereoselectivity-from concepts to quantitative calculations and predictions,* (2016).

[57] J. P. Perdew and Y. Wang, *Accurate and simple analytic representation of the electron-gas correlation energy,* Physical Review B **45**, 13244 (1992).

[58] J. P. Perdew, K. Burke, and M. Ernzerhof, *Generalized gradient approximation made simple,* Phys. Rev. Lett. **77**, 3865 (1996).

[59] S. Clark, *DFT: Exchange-Correlation,* University of Durham .

[60] Z. G. Yu, J. Sun, M. B. Sullivan, Y. W. Zhang, H. Gong, and D. J. Singh, *Dopant chemical potential modulation on oxygen vacancies formation in In2O3: A comparative density functional study,* Chemical Physics Letters **621**, 141 (2015).

[61] P. Ágoston, C. Körber, A. Klein, M. J. Puska, R. M. Nieminen, and K. Albe, *Limits for n -type doping in In2 O3 and SnO 2: A theoretical approach by first-principles calculations using hybrid-functional methodology,* Journal of Applied Physics **108** (2010), 10.1063/1.3467780.

[62] J. P. Perdew and M. Levy, *Physical content of the exact kohn-sham orbital energies: Band gaps and derivative discontinuities,* Phys. Rev. Lett. **51**, 1884 (1983).

[63] J. P. Perdew, *Density functional theory and the band gap problem,* International Journal of Quantum Chemistry **28**, 497 (1985).

[64] J. Heyd, G. E. Scuseria, and M. Ernzerhof, *Hybrid functionals based on a screened Coulomb potential,* Journal of Chemical Physics **118**, 8207 (2003).

[65] M. Ramzan, Y. Li, and R. Ahuja, *Electronic structure, mechanical and optical properties of In 2O3 with hybrid density functional (HSE06),* Solid State Communications **172**, 37 (2013).

[66] L. Lutterotti, *Introduction to Crystallography Diffraction Techniques*, Tech. Rep.

[67] J. Martínez-Duart, R. Martín-Palma, and F. Agulló-Rueda, *Survey of Solid State Physics,* in *Nanotechnology for Microelectronics and Optoelectronics* (Elsevier, 2006) pp. 21–53.

[68] M. Asta, *Integrated Computational Materials Engineering Education Lecture on Density Functional Theory An Introduction,* .

[69] P. K. Misra, *Basic Properties of Crystals,* in *Physics of Condensed Matter* (Elsevier, 2012) pp. 1–35.

[70] A. Kahn, *Fermi level, work function and vacuum level,* Materials Horizons **3**, 7 (2016).

[71] J. Petzelt and I. Rychetskỳ, *Dielectric Function,* in *Encyclopedia of Condensed Matter Physics* (Elsevier Inc., 2005) pp. 426–429.

[72] P. Rani, G. S. Dubey, and V. K. Jindal, *DFT study of optical properties of pure and doped Graphene Department of Earth & Physical Sciences , York College of City University of New York ,,* arXiv , 1.

[73] *The Kramers-Kronig Relations,* in *The Physics of Thin Film Optical Spectra* (Springer-Verlag, 2005) pp. 61–68.

[74] F. Wooten, *Optical properties of solids,* Academic Press (1972).

[75] B. I. Bleaney and B. Bleaney, *Electricity and magnetism, 3rd ed., Oxford University Press, Oxford,* (1994).

[76] M. Nishiwaki and H. Fujiwara, *Highly accurate prediction of material optical properties based on density functional theory,* Computational Materials Science **172**, 109315 (2020).

[77] J. Müller, B. Rech, J. Springer, and M. Vanecek, *TCO and light trapping in silicon thin film solar cells,* Solar Energy **77**, 917 (2004).

[78] M. Dressel and M. Scheffler, *Verifying the Drude response,* Annalen der Physik **15**, 535 (2006).

[79] I. Hamberg, C. G. Granqvist, K. F. Berggren, B. E. Sernelius, and L. Engström, *Band-gap widening in heavily Sn-doped In2O3,* Physical Review B **30**, 3240 (1984).

[80] M. Marezio, *Refinement of the crystal structure of In 2 O 3 at two wavelengths ,* Acta Crystallographica **20**, 723 (1966).

[81] P. Reunchan, X. Zhou, S. Limpijumnong, A. Janotti, and C. G. Van De Walle, *Vacancy defects in indium oxide: An ab-initio study,* in *Current Applied Physics*, Vol. 11 (North-Holland, 2011) pp. S296–S300.

[82] K. Persson, *Materials data on in2o3 (sg:206) by materials project,* (2014).

[83] L. Bizo, J. Choisnet, R. Retoux, and B. Raveau, *The great potential of coupled substitutions in In2O3 for the generation of bixbyite-type transparent conducting oxides, In 2-2xMxSnxO3,* Solid State Communications **136**, 163 (2005).

[84] K. Momma and F. Izumi, *VESTA 3 for three-dimensional visualization of crystal, volumetric and morphology data,* Journal of Applied Crystallography **44**, 1272 (2011).

[85] A. Walsh, J. L. Da Silva, S. H. Wei, C. Körber, A. Klein, L. F. Piper, A. Demasi, K. E. Smith, G. Panaccione, P. Torelli, D. J. Payne, A. Bourlange, and R. G. Egdell, *Nature of the band gap of In2O3 revealed by first-principles calculations and X-ray spectroscopy,* Physical Review Letters **100**, 2 (2008).

[86] P. D. King, T. D. Veal, F. Fuchs, C. Y. Wang, D. J. Payne, A. Bourlange, H. Zhang, G. R. Bell, V. Cimalla, O. Ambacher, R. G. Egdell, F. Bechstedt, and C. F. McConville, *Band gap, electronic structure, and surface electron accumulation of cubic and rhombohedral In2 O3,* Physical Review B - Condensed Matter and Materials Physics **79**, 1 (2009).

[87] H. J. Monkhorst and J. D. Pack, *Special points for Brillouin-zone integrations,* Physical Review B **13**, 5188 (1976).

[88] H. Ibach and H. Lüth, *The Electronic Bandstructure of Solids,* in *Solid-State Physics* (Springer Berlin Heidelberg, 2009) pp. 159–189.

[89] Y. Hinuma, G. Pizzi, Y. Kumagai, F. Oba, and I. Tanaka, *Band structure diagram paths based on crystallography,* Computational Materials Science **128**, 140 (2017), arXiv:1602.06402 .

[90] H. A. Aliabad, M. Bazrafshan, H. Vaezi, M. Yousaf, J. Munir, and M. A. Saeed, *Optoelectronic properties of pure and Co doped indium oxide by hubbard and modified becke-johnson exchange potentials,* Chinese Physics Letters **30** (2013), 10.1088/0256-307X/30/12/127101.

[91] E. Aydin, M. De Bastiani, X. Yang, M. Sajjad, F. Aljamaan, Y. Smirnov, M. N. Hedhili, W. Liu, T. G. Allen, L. Xu, E. Van Kerschaver, M. Morales-Masis, U. Schwingenschlögl, and S. De Wolf, *Zr-Doped Indium Oxide (IZRO) Transparent Electrodes for Perovskite-Based Tandem Solar Cells,* Advanced Functional Materials **29**, 1 (2019).

[92] D. R. Hagleitner, P. Jacobson, S. Blomberg, K. Schulte, E. Lundgren, M. Kubicek, J. Fleig, F. Kubel, C. Puls, A. Limbeck, H. Hutter, L. A. Boatner, M. Schmid, and U. Diebold, *Bulk and surface characterization of In2O3(001) single crystals,* arXiv **3**, 1 (2018).

[93] I. Hamberg and C. G. Granqvist, *Evaporated Sn-doped In2O3 films: Basic optical properties and applications to energy-efficient windows,* Journal of Applied Physics **60** (1986), 10.1063/1.337534.

[94] R. F. Minibaev, A. A. Bagatur'yants, D. I. Bazhanov, A. A. Knizhnik, and M. V. Alfimov, *First-principles investigation of the electron work function for the (001) surface of indium oxide In2O3 and indium tin oxide (ITO) as a function of the surface oxidation level,* Nanotechnologies in Russia **5**, 185 (2010).

[95] C. A. Pan and T. P. Ma, *Work function of In2O3 film as determined from internal photoemission,* Applied Physics Letters **37**, 714 (1980).

[96] W. G. Thompson and R. L. Anderson, *Electrical and photovoltaic characteristics of indium-tin oxide/silicon heterojunctions,* Solid State Electronics **21**, 603 (1978).

[97] R. L. Weiher and R. P. Ley, *Optical properties of indium oxide,* Journal of Applied Physics **37**, 299 (1966).

[98] F. Matino, L. Persano, V. Arima, D. Pisignano, R. I. Blyth, R. Cingolani, and R. Rinaldi, *Electronic structure of indium-tin-oxide films fabricated by reactive electron-beam deposition,* Physical Review B - Condensed Matter and Materials Physics **72**, 085437 (2005).

[99] L. Gupta, A. Mansingh, and P. K. Srivastava, *Band gap narrowing and the band structure of tin-doped indium oxide films,* Thin Solid Films **176**, 33 (1989).

[100] D. S. Bhachu, D. O. Scanlon, G. Sankar, T. D. Veal, R. G. Egdell, G. Cibin, A. J. Dent, C. E. Knapp, C. J. Carmalt, and I. P. Parkin, *Origin of high mobility in molybdenum-doped indium oxide,* Chemistry of Materials **27**, 2788 (2015).

[101] G. G. Untila, T. N. Kost, and A. B. Chebotareva, *Fluorine doped indium oxide films for silicon solar cells,* Thin Solid Films **518**, 1345 (2009).

[102] C. Han, L. Mazzarella, Y. Zhao, G. Yang, P. Procel, M. Tijssen, A. Montes, L. Spitaleri, A. Gulino, X. Zhang, O. Isabella, and M. Zeman, *High-Mobility Hydrogenated Fluorine-Doped Indium Oxide Film for Passivating Contacts c-Si Solar Cells,* ACS Applied Materials and Interfaces **11**, 45586 (2019).

[103] J. S. Seo, J. H. Jeon, Y. H. Hwang, H. Park, M. Ryu, S. H. K. Park, and B. S. Bae, *Solution-processed flexible fluorine-doped indium zinc oxide thin-film transistors fabricated on plastic film at low temperature,* Scientific Reports **3**, 1 (2013).

[104] E. Shanthi, A. Banerjee, V. Dutta, and K. L. Chopra, *Electrical and optical properties of tin oxide films doped with F and (Sb+F),* Journal of Applied Physics **53**, 1615 (1982).

[105] M. Jaccaud, R. Faron, D. Devilliers, R. Romano, S. Riedel, and H. Pernice, *Fluorine,* in *Ullmann's Encyclopedia of Industrial Chemistry* (Wiley, 2000) pp. 1–19.

[106] Y. Zhang, *Electronegativities of Elements in Valence States and Their Applications. 2. A Scale for Strengths of Lewis Acids,* Inorganic Chemistry **21**, 3889 (1982).

[107] Z. Lu, F. Meng, Y. Cui, J. Shi, Z. Feng, Z. Liu, Z. Lu, F. Meng, Y. Cui, J. Shi, Z. Feng, and Z. Liu, *High quality of IWO films prepared at room temperature by reactive plasma deposition for photovoltaic devices,* JPhD **46**, 075103 (2013).

[108] H. C. Lee, *Electron scattering mechanisms in indium-tin-oxide thin films prepared at the various process conditions,* Applied Surface Science **252**, 3428 (2006).

[109] O. Bierwagen and J. S. Speck, *Mg acceptor doping of In2O3 and overcompensation by oxygen vacancies,* Applied Physics Letters **101**, 102107 (2012).

[110] S. Limpijumnong, P. Reunchan, A. Janotti, and C. G. V. de Walle, *Hydrogen doping in indium oxide: An <i>ab initio</i> study,* Physical Review B **80**, 193202 (2009).

[111] M. Morales-Masis, S. M. D. Nicolas, J. Holovský, S. D. Wolf, and C. Ballif, *Low-Temperature High-Mobility Amorphous IZO for Silicon Heterojunction Solar Cells,* IEEE journal of photovoltaics **5**, 1340 (2015).

[112] K. Nomura, H. Ohta, A. Takagi, T. Kamiya, M. Hirano, and H. Hosono, *Room-temperature fabrication of transparent flexible thin-film transistors using amorphous oxide semiconductors,* Nature 2004 432:7016 **432**, 488 (2004).